CHAPTER 12

Extremely Large Deformation with Polygonal and Polyhedral Elements*

Glaucio H. Paulino, Heng Chi

Georgia Institute of Technology, Atlanta, USA

Cameron Talischi

McKinsey & Company, Chicago, USA

Oscar Lopez-Pamies

University of Illinois at Urbana-Champaign, USA

CONTENTS

*Research support from the U.S. National Science Foundation through grant CMMI #1624232 (formerly #1437535) is gratefully acknowledged. The information presented in this chapter is the sole opinion of the authors and does not necessarily reflect the views of the sponsoring agency.

Soft organic materials are of great engineering interest, but challenging to model with standard finite elements. The challenges arise primarily because their nonlinear elastic response is characterized by non-convex stored-energy functions, they are incompressible or nearly incompressible, and oftentimes possess complex microstructures. Recently, polygonal finite elements have been found to possess several advantages over standard finite elements when studying the mechanics of such materials under finite deformations. This chapter summarizes a new approach, using polygonal and polyhedral elements in nonlinear elasticity problems involving extremely large and heterogeneous deformations. We present both displacement-based and two-field mixed variational principles for finite elasticity, together with the corresponding lower- and higher-order polygonal and polyhedral finite element approximations. We also utilize a gradient correction scheme that adds minimal perturbations to the gradient field at the element level in order to restore polynomial consistency and recover (expected) optimal convergence rates when the weak form integrals are evaluated using quadrature rules. With the gradient correction scheme, optimal convergence of the numerical solutions for displacement-based and mixed formulations with both lower- and higher-order displacement interpolants is confirmed by numerical studies of several boundary-value problems in finite elasticity. For demonstration purposes, we deploy the proposed polygonal discretization to study the nonlinear elastic response of rubber filled with random distributions of rigid particles considering interphasial effects. These physically motivated examples illustrate the potential of polygonal finite elements to simulate the nonlinear elastic response of soft organic materials with complex microstructures under finite deformations.

12.1 INTRODUCTION

Many organic materials are characterized by their ability to undergo large reversible deformations in response to a variety of stimuli, including mechanical forces, electric and magnetic fields, and temperature changes. While they have long been utilized in numerous engineering applications, modern advances in material science have demonstrated that soft organic materials, such as electro- and magneto-active elastomers, gels, and shape-memory polymers, hold tremendous potential to enable new technologies, and in particular, the new generation of sensors and actuators. From a mechanical perspective, although most of these materials can be approximated "simply" as nonlinear elastic, they more often than not contain highly heteroge-

neous, complex microstructures. The heterogeneity of the microstructures makes the underlying local deformations inherently complex.

Computational microscopic studies of nonlinear elastic materials, especially those with complex microstructures, help in gaining a quantitative understanding of the complex behavior of these materials. These studies are also essential in guiding the optimization of nonlinear elastic materials, so that they can enable new technological applications. It has long been recognized that standard finite elements, especially simplicial (triangular and tetrahedral) finite elements, are inadequate in simulating processes involving realistic, large deformations—an example is shown in Figure 12.1. By contrast, recent studies have demonstrated that polygonal elements possess significant potential in the study of nonlinear elastic materials under finite deformations. First, these elements are well-suited to model complex microstructures (e.g., particulate microstructures and microstructures involving different length scales) and to seamlessly incorporate periodic boundary conditions. Secondly, polygonal elements are found to be more tolerant to large localized deformations and to produce more accurate results in bending and shear than standard finite elements. With mixed formulations, lower-order mixed polygonal elements are also shown to be numerically stable on Voronoi-type meshes without the need for any additional stablization terms. Likewise, numerical stability of the polygonal finite elements is also demonstrated in topology optimization [160, 389, 392] and in fluid mechanics [394] problems.

One major challenge in the polygonal finite method is accurate numerical integration of the weak-form integrals. The finite element space for polygonal elements contains non-polynomial (e.g., rational) functions, and therefore, the use of existing quadrature schemes, typically designed for integration of polynomial functions, leads to non-vanishing consistency errors [268, 388] and consequently, sub-optimal or even non-convergent finite element solutions under mesh refinement. In practice, using a sufficiently large number of integration points can lower the consistency error for linear polygonal elements in two dimensions. A triangulation scheme with three integration points per triangle is shown to be sufficiently accurate for practical problems and mesh sizes [99, 388]. However, for higher-order polygonal elements, the number of integration points for such a scheme can become prohibitively large [100]. This is also the case for polyhedral elements in three dimensions [268, 393]. In practical applications, as the number of elements increases, the associated computational cost for a polyhedral discretization can become exorbitant.

Several attempts have been made in the literature to address the issue of numerical quadrature. For example, in the context of scalar diffusion problems, inspired by the virtual element method (VEM) [33, 72, 161], Talischi et al. [388] have proposed a polynomial projection approach to ensure the polynomial consistency of the bilinear form, and thereby ensure the satisfaction of the patch test and optimal convergence for both linear and quadratic polygonal elements. A similar approach was also adopted by Manzini et al. [268] to solve Poisson problems on polyhedral meshes. However, those approaches require the existence of a bilinear form, and therefore, extension to general nonlinear problems is non-trivial and is still an open question. Borrowing the idea of pseudo-derivatives in the meshfree literature [229],

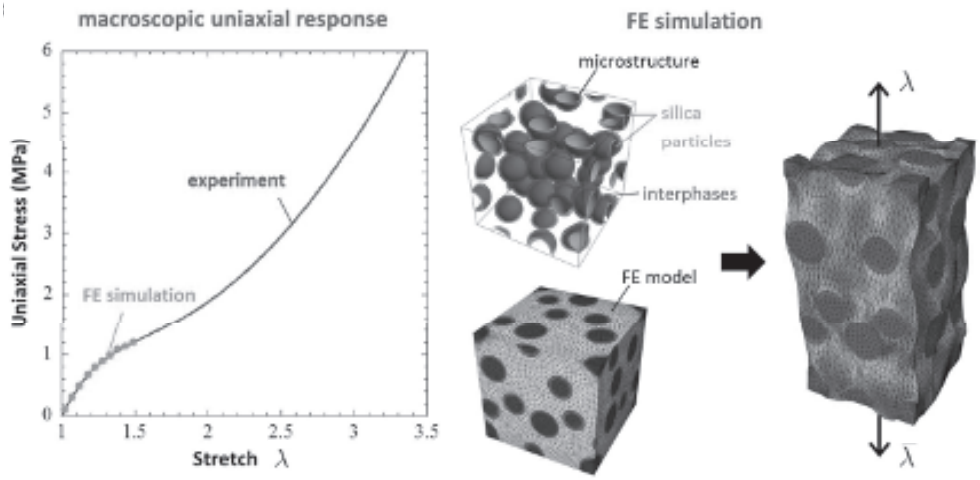

Figure 12.1 An illustration of the limited capability of standard tetrahedral elements to undergo large deformation. Experimentally, a synthetic rubber filled with 20% volume fraction of randomly distributed silica particles can be stretched more than four times its original length ($\lambda = 4$) without internal damage under uniaxial tension [315]. By contrast, a finite element model, based on standard 10-node hybrid elements with linear pressure, is only able to deform to a macroscopic stretch of $\lambda = 1.5$ [174]. See color insert.

Bishop has proposed an approach to correct the derivatives of the shape functions to enforce the linear consistency property on general polygonal and polyhedral meshes [46, 47]. With this correction, the linear patch test is passed and optimal convergence is achieved. Although applicable for general nonlinear scenarios, the extension to higher-order cases (for example, quadratic polygonal finite elements) is not straightforward, More recently, Talischi et al. [393] proposed a general gradient correction scheme that is applicable to both linear and nonlinear problems on arbitrary-order polygonal and polyhedral elements. By requiring a minimum order of accuracy in the numerical quadrature, the correction scheme is shown to restore optimal convergence for both linear and nonlinear problems [393]. In this chapter, we apply the gradient correction scheme to polygonal and polyhedral finite elements for finite elasticity problems and demonstrate that the gradient correction scheme can effectively and efficiently render optimally convergent polygonal and polyhedral finite element methods.

12.2 FINITE ELASTICITY FORMULATIONS

This section briefly recalls the equations of elastostatics applied to hyperelastic materials. Two variational formulations are presented: (i) the standard displacement-based formulation [63, 294, 429], and (ii) a general mixed formulation involving the

displacement field and a pressure-like scalar field as trial fields. Throughout this chapter, we adopt a Lagrangian description of the fields.

Consider a body in its stress-free, undeformed configuration that occupies an open domain $\Omega \subset \mathbb{R}^d$ with boundary $\partial\Omega$. On its boundary, it is subjected to a prescribed displacement field $\boldsymbol{u}^0$ on $\Gamma^{\boldsymbol{x}}$ and traction $\boldsymbol{t}$ (per unit undeformed surface) on $\Gamma^{\boldsymbol{t}}$, such that $\Gamma^{\boldsymbol{x}} \cup \Gamma^{\boldsymbol{t}} = \partial\Omega$ and $\Gamma^{\boldsymbol{x}} \cap \Gamma^{\boldsymbol{t}} = \varnothing$. The body is also assumed to be subjected to a body-force $\boldsymbol{f}$ (per unit undeformed volume) in Ω. A stored-energy function W is used to characterize the constitutive behavior of the body, which is assumed to be an objective function of the deformation gradient $\boldsymbol{F}$. In terms of W, the first Piola–Kirchhoff stress tensor $\boldsymbol{P}$ at each material point $\boldsymbol{x} \in \Omega$ is thus given by the following relation:

$$\boldsymbol{P}(\boldsymbol{x}) = \frac{\partial W}{\partial \boldsymbol{F}}(\boldsymbol{x}, \boldsymbol{F}),$$

which is used as the stress measure of choice in this chapter.

12.2.1 Displacement-based formulation

The well-known principle of minimum potential energy asserts that the equilibrium displacement field $\boldsymbol{u}$ minimizes the potential energy Π among all displacement fields that are kinematically admissible:

$$\Pi(\boldsymbol{u}) = \min_{\boldsymbol{v} \in \mathcal{K}} \Pi(\boldsymbol{v}), \tag{12.1}$$

with

$$\Pi(\boldsymbol{v}) = \int_\Omega W(\boldsymbol{x}, \boldsymbol{F}(\boldsymbol{v}))\, d\boldsymbol{x} - \int_\Omega \boldsymbol{f} \cdot \boldsymbol{v}\, d\boldsymbol{x} - \int_{\Gamma^{\boldsymbol{t}}} \boldsymbol{t} \cdot \boldsymbol{v}\, ds. \tag{12.2}$$

In the above expression, $\mathcal{K}$ stands for a sufficiently large set of displacements such that $\boldsymbol{v} = \boldsymbol{u}^0$ on $\Gamma^{\boldsymbol{x}}$.

The weak form of the Euler–Lagrange equations associated with the variational problem (12.1) reads as follows:

$$\begin{aligned} G(\boldsymbol{v}, \delta\boldsymbol{v}) = \int_\Omega \frac{\partial W}{\partial \boldsymbol{F}}(\boldsymbol{x}, \boldsymbol{F}(\boldsymbol{v})) : \nabla(\delta\boldsymbol{v})\, d\boldsymbol{x} - \int_\Omega \boldsymbol{f} \cdot \delta\boldsymbol{v}\, d\boldsymbol{x} \\ - \int_{\Gamma^{\boldsymbol{t}}} \boldsymbol{t} \cdot \delta\boldsymbol{v}\, ds = 0 \quad \forall \delta\boldsymbol{v} \in \mathcal{K}^0, \end{aligned} \tag{12.3}$$

where the test displacement field $\delta\boldsymbol{v}$ is the variation of $\boldsymbol{v}$, and $\mathcal{K}^0$ denotes the set of all the kinematically admissible displacement fields that vanish on $\Gamma^{\boldsymbol{x}}$.

12.2.2 A general two-field mixed variational formulation

For nonlinear elastic materials that are nearly incompressible, the variational principle in (12.1)–(12.2) is known to perform poorly when approximated by standard finite element methods [204]. As a standard remedy, mixed variational principles that involve not only the deformation, but also a pressure field are utilized [17, 75, 87, 90, 99, 188, 362, 385]. Based on the multiplicative splitting of

the deformation gradient, the mixed variational formulations are categorized into two classes, the $\boldsymbol{F}$-formulation and the $\overline{\boldsymbol{F}}$-formulation [99]. In this section, we recall the $\boldsymbol{F}$-formulation; for the $\overline{\boldsymbol{F}}$-formulation, the reader is referred to [17, 99, 188] and references therein.

The basic idea is to introduce a function $\widehat{W}$ such that $W(\boldsymbol{x}, \boldsymbol{F}) = \widehat{W}(\boldsymbol{x}, \boldsymbol{F}, J)$ when $J = \det \boldsymbol{F}$, and its partial Legendre transformation,

$$\widehat{W}^*(\boldsymbol{x}, \boldsymbol{F}, \widehat{q}) = \max_J \big\{ \widehat{q}(J-1) - \widehat{W}(\boldsymbol{x}, \boldsymbol{F}, J) \big\}.$$

Provided that $\widehat{W}$ is convex in the argument J, the following duality relation holds:

$$\widehat{W}(\boldsymbol{x}, \boldsymbol{F}, J) = \max_{\widehat{q}} \big\{ \widehat{q}(J-1) - \widehat{W}^*(\boldsymbol{x}, \boldsymbol{F}, \widehat{q}) \big\}. \tag{12.4}$$

Direct substitution of relation (12.4) in the principle of minimum potential energy (12.1)–(12.2) renders the following alternative mixed variational principle:

$$\widehat{\Pi}(\boldsymbol{u}, \widehat{p}) = \min_{\boldsymbol{v} \in \mathcal{K}} \max_{\widehat{q} \in \mathcal{Q}} \widehat{\Pi}(\boldsymbol{v}, \widehat{q}), \tag{12.5}$$

with

$$\begin{aligned} \widehat{\Pi}(\boldsymbol{v}, \widehat{q}) \quad = \quad & \int_\Omega \big\{ -\widehat{W}^*(\boldsymbol{x}, \boldsymbol{F}(\boldsymbol{v}), \widehat{q}) + \widehat{q}[\det \boldsymbol{F}(\boldsymbol{v}) - 1] \big\} \, d\boldsymbol{x} \\ & - \int_\Omega \boldsymbol{f} \cdot \boldsymbol{v} \, d\boldsymbol{x} - \int_{\Gamma^{\boldsymbol{t}}} \boldsymbol{t} \cdot \boldsymbol{v} \, ds. \end{aligned} \tag{12.6}$$

In the above expression, $\mathcal{Q}$ denotes the set of square-integrable scalar functions and the maximizing scalar field $\widehat{p}$ is directly related to the equilibrium Cauchy hydrostatic pressure field $p := \operatorname{tr} \boldsymbol{\sigma}$ via [99]

$$p = \widehat{p} - \frac{1}{3 \det \boldsymbol{F}} \frac{\partial \widehat{W}^*}{\partial \boldsymbol{F}}(\boldsymbol{x}, \boldsymbol{F}, \widehat{p}) : \boldsymbol{F}.$$

The weak form of the Euler–Lagrange equations associated with the variational principle (12.5)–(12.6) reads as

$$\begin{aligned} G^{\boldsymbol{v}}(\boldsymbol{v}, \widehat{q}, \delta\boldsymbol{v}) = \int_\Omega \left[-\frac{\partial \widehat{W}^*}{\partial \boldsymbol{F}}(\boldsymbol{x}, \boldsymbol{F}(\boldsymbol{v}), \widehat{q}) + \widehat{q} \operatorname{adj}\big(\boldsymbol{F}^T(\boldsymbol{v})\big) \right] : \nabla(\delta\boldsymbol{v}) \, d\boldsymbol{x} \\ - \int_\Omega \boldsymbol{f} \cdot \delta\boldsymbol{v} \, d\boldsymbol{x} - \int_{\Gamma^{\boldsymbol{t}}} \boldsymbol{t} \cdot \delta\boldsymbol{v} \, ds = 0 \qquad \forall \delta\boldsymbol{v} \in \mathcal{K}^0, \end{aligned}$$

$$G^{\widehat{q}}(\boldsymbol{v}, \widehat{q}, \delta\widehat{q}) = \int_\Omega \left[\det \boldsymbol{F}(\boldsymbol{v}) - 1 - \frac{\partial \widehat{W}^*}{\partial \widehat{q}}(\boldsymbol{x}, \boldsymbol{F}(\boldsymbol{v}), \widehat{q}) \right] \delta\widehat{q} \, d\boldsymbol{x} = 0 \qquad \forall \delta\widehat{q} \in \mathcal{Q},$$

where the test field $\delta\widehat{q}$ is the variation of $\widehat{q}$, and $\operatorname{adj}(\cdot)$ stands for the adjugate operator.

12.3 POLYGONAL AND POLYHEDRAL APPROXIMATIONS

This section discusses the displacement and pressure spaces for the polygonal and polyhedral finite element approximations. In 2D, we present the constructions of conforming finite-dimensional displacement and pressure spaces, for both linear and quadratic polygonal finite elements. In 3D, we present the construction of linear displacement finite element space on convex polyhedra.

12.3.1 Displacement space on polygons in 2D

Let us begin in the 2D setting and consider a general polygon P with n edges and vertices, $\boldsymbol{v}_1, \ldots, \boldsymbol{v}_n$, in the undeformed configuration. We use generalized barycentric coordinates as the basis for a linear polygonal finite element space on P, denoted by $\mathcal{V}_1(P)$, with degrees of freedom associated with the vertices of P.

Quite a few barycentric coordinates can be found in the literature [15, 34, 149, 193, 215, 265, 275, 372] (see Chapter 1 for details), among which the mean value coordinates [144] are adopted in this chapter. The mean value coordinates, denoted by $\phi_1^{(1)}, \ldots, \phi_n^{(1)}$, can be constructed on arbitrary polygons. Contour plots of the mean value coordinates defined on non-convex polygons are shown in Figure 12.2(a).

A second-order space on P, denoted as $\mathcal{V}_2(P)$, can be constructed using pairwise products of the generalized barycentric coordinates [320]. $\mathcal{V}_2(P)$ is a $2n$-dimensional space having the degrees of freedom at each vertex of P, as well as at the mid-point of each edge. Its interpolants $\phi_1^{(2)}, \ldots, \phi_{2n}^{(2)}$ are expressed as:

$$\phi_i^{(2)}(\boldsymbol{x}) = \sum_{j=1}^{n} \sum_{l=1}^{n} c_{jl}^i \phi_j^{(1)}(\boldsymbol{x}) \phi_l^{(1)}(\boldsymbol{x}),$$

where $\phi_j^{(1)}$ are the mean value coordinates. The coefficients c_{jl}^i are computed such

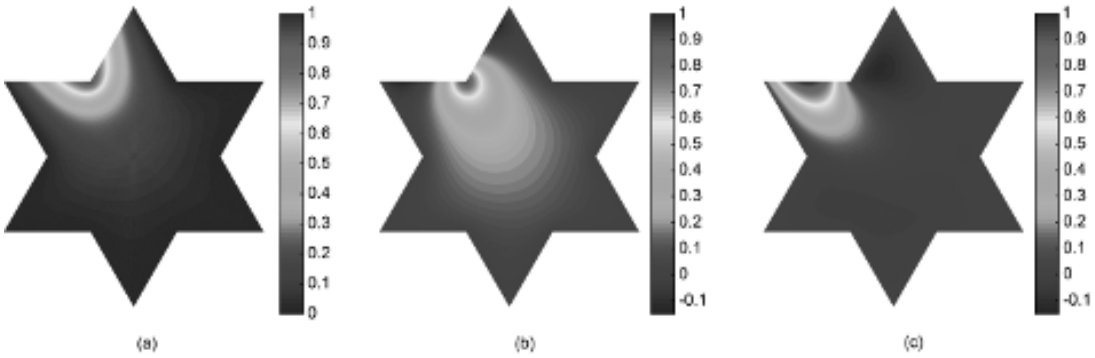

Figure 12.2 (a) Contour plot of a mean value basis $\phi_i^{(1)}$ over a concave polygon. (b) Contour plot of quadratic basis $\phi_i^{(2)}$ over a concave polygon associated with a vertex. (c) Contour plot of quadratic basis $\phi_i^{(2)}$ over a concave polygon associated with a mid-side node. See color insert.

that any quadratic function can be interpolated exactly by $\phi_i^{(2)}$:

$$q(\boldsymbol{x}) = \sum_{i=1}^{n} \left[q(\boldsymbol{v}_i)\phi_i^{(2)}(\boldsymbol{x}) + q(\hat{\boldsymbol{v}}_i)\phi_{i+n}^{(2)}(\boldsymbol{x}) \right] \quad \forall q \in \mathcal{P}_2(E),$$

and the Kronecker-delta property

$$\phi_i^{(2)}(\boldsymbol{v}_j) = \phi_{i+n}^{(2)}(\hat{\boldsymbol{v}}_j) = \delta_{ij}, \quad \phi_i^{(2)}(\hat{\boldsymbol{v}}_j) = \phi_{i+n}^{(2)}(\boldsymbol{v}_j) = 0 \quad \forall i, j = 1, \ldots, n,$$

is satisfied, where $\hat{\boldsymbol{v}}_i = (\boldsymbol{v}_i + \boldsymbol{v}_{i+1})/2$ denotes the mid-side nodes.

Although the construction above is derived assuming that the polygonal elements are strictly convex [320], we also find that it is valid on concave polygons when constructed from the mean value coordinates. Basis function plots for a vertex node and a mid-side node of a concave polygon are shown in Figures 12.2(b) and 12.2(c), respectively.

12.3.2 Displacement space on polyhedra in 3D

Let $P \in \mathbb{R}^3$ be a polyhedron whose boundary consists of planar polygonal faces in its undeformed configuration with its n vertices located at $\boldsymbol{v}_1, \ldots, \boldsymbol{v}_n$. As in the 2D case, one can define generalized barycentric coordinates $\phi_1^{(1)}, \ldots, \phi_n^{(1)}$ as the basis for a linear polyhedral finite element space on P using vertex degrees of freedom.

This chapter considers the Wachspress coordinates, as defined in [413] and analyzed in [147], which are valid for simple polyhedra. This means that the collection of faces that include $\boldsymbol{v}$ for each $i = 1, \ldots, n$ consists of exactly three faces. As before, we denote by $\mathcal{V}_1(P) = \text{span}\{\phi_1^{(1)}, \ldots, \phi_n^{(1)}\}$ the finite element space on P, which by linear precision of the Wachspress coordinates includes $\mathcal{P}_1(P)$. We remark that the gradient correction scheme described later in this chapter is applicable to other types of coordinates on linear and quadratic polyhedrons as well, though certain aspects of its implementation and performance in numerical simulations require a separate examination.

12.3.3 Pressure space on polygons in 2D

Regarding the two-field mixed finite elements, approximation of the additional pressure field is needed. This chapter only considers mixed polygonal elements in 2D; we leave mixed polyhedral elements as a subject for future work. For conforming approximations of $\mathcal{Q}$, either discontinuous or continuous approximations can be adopted. For discontinuous approximations, the discrete pressure space $\mathcal{Q}_{h,k-1}^D$ can be defined as:

$$\mathcal{Q}_{h,k-1}^D = \{\widehat{q}_h \in \mathcal{Q} : \widehat{q}_h|_P \in \mathcal{P}_{k-1}(P)\ \forall P \in \Omega_h\},$$

where k is the order of the element. As implied by the above definition, the approximated pressure field may be discontinuous across element boundaries. This type

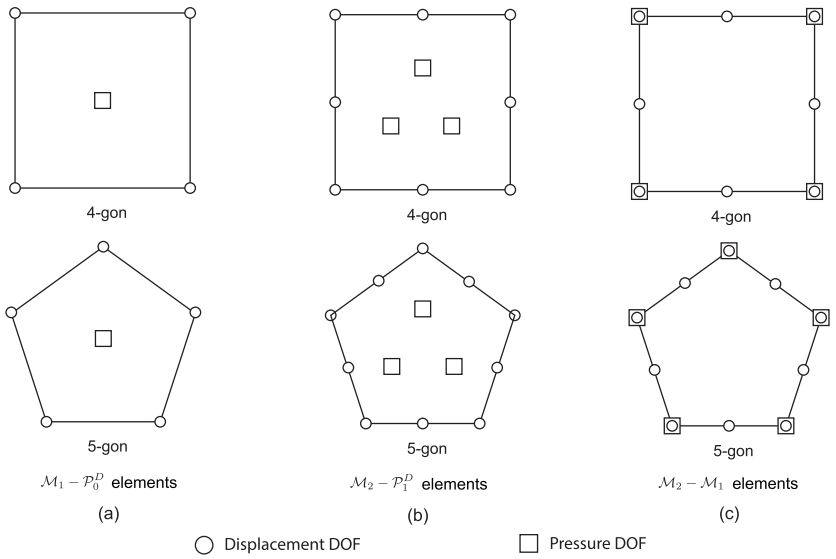

Figure 12.3 Illustration of the degrees of freedom of displacement and pressure fields for different mixed polygonal elements. (a) $\mathcal{M}_1 - \mathcal{P}_0^D$ elements, (b) $\mathcal{M}_2 - \mathcal{P}_1^D$ elements, and (c) $\mathcal{M}_2 - \mathcal{M}_1$ elements.

of mixed element is similar to the Crouzeix–Raviart (C–R) elements in fluid problems [110]. For the remainder of this chapter, we adapt the acronyms from [100] and denote this family of mixed elements as $\mathcal{M}_k - \mathcal{P}_{k-1}^D$ elements. Therefore, the pressure space of the $\mathcal{M}_1 - \mathcal{P}_0^D$ element consists of piecewise constant functions, which are constant over each element. Similarly, the pressure space of the $\mathcal{M}_2 - \mathcal{P}_1^D$ element contains piecewise linear functions that vary linearly over each element.

Alternatively, a continuous approximation of the pressure space can be defined in the following manner:

$$\mathcal{Q}_{h,k-1}^C = \{\widehat{q}_h \in C^0(\Omega) : \widehat{q}_h|_P \in \mathcal{M}_{k-1}(P) \; \forall P \in \Omega_h\}.$$

This class of elements resembles the Taylor-Hood (T–H) elements in fluid problems [395], and they are henceforth denoted as the $\mathcal{M}_k - \mathcal{M}_{k-1}$ elements ($k \geq 2$).

Here we consider both types of mixed polygonal finite elements up to quadratic order. As an illustration, the degrees of freedom (DOFs) of the displacement field and pressure field for these mixed polygonal elements are shown in Figure 12.3.

12.4 QUADRATURE RULES AND ACCURACY REQUIREMENTS

On general polygonal and polyhedral elements, generalized barycentric coordinates are usually non-polynomial functions. As discussed in [100, 388, 393], the evaluation of weak form integrals involving barycentric coordinates and their gradients by means of available quadrature schemes leads to errors that are persistent under mesh refinement. In order to control the quadrature errors and restore polynomial

consistency, using the gradient correction scheme by Talischi et al. [393] requires the quadrature schemes that are adopted to respect certain minimal accuracy requirements, which are expressed in terms of their polynomial precision. In this section, we state these requirements for volumetric and surface quadrature rules on a general element P and proceed to introduce the numerical quadrature schemes that are used.

Given a polygonal or polyhedral finite element P, we denote by $\fint_P$ the evaluation of the volume (area) integral $\int_P$ using quadrature. Similarly, we use $\oint_{\partial P}$ to denote the numerical evaluation of surface (line) integral $\int_{\partial P}$. Throughout, we shall assume that the order k of the finite element space $\mathcal{V}_k(P)$ is fixed.

In the gradient correction scheme by Talischi et al. [393], the volumetric quadrature $\fint_P$ is assumed to be exact when the integrand is a polynomial field of order $2k-2$. This means that the quadrature can exactly integrate constant fields when $k=1$ and quadratic fields when $k=2$. This requirement guarantees that the integrals,

$$\int_P \boldsymbol{p}\cdot\nabla q\, d\boldsymbol{x}, \qquad \int_P q\nabla\cdot\boldsymbol{p}\, d\boldsymbol{x},$$

are exact when $\boldsymbol{p}\in[\mathcal{P}_{k-1}(P)]^d$ and $q\in\mathcal{P}_k(P)$. Additionally, an implicit assumption is made on the volume quadrature rule that it is sufficiently rich to eliminate the appearance of spurious elemental zero-energy modes that can compromise the stability of the resulting discretization scheme. For instance, for $k=1$, a one-point rule consisting of an integration point at the centroid of E, with the volume $|P|$ being the weight, satisfies the above precision requirement, but leads to spurious zero-energy modes.

On the other hand, the boundary quadrature $\oint_{\partial P}$ is required to integrate polynomial fields of order $2k-1$ on each edge/face of the element. Therefore, 1-point ($k=1$) and 2-point ($k=2$) quadrature suffices for piecewise linear and cubic fields, respectively. This requirement ensures that integrals of the form

$$\int_{\partial P} q(\boldsymbol{p}\cdot\boldsymbol{n})ds$$

are exact if $\boldsymbol{p}\in[\mathcal{P}_{k-1}(P)]^d$ and q are piecewise k-th order polynomials on ∂P with $\boldsymbol{n}$ being the unit normal vector to the boundary. For 2D elements, because the functions in $\mathcal{V}_k(P)$ have k-th order polynomial variation on ∂P, the assumed accuracy ensures exact integration:

$$\oint_{\partial P} v(\boldsymbol{p}\cdot\boldsymbol{n})\, ds = \int_{\partial P} v(\boldsymbol{p}\cdot\boldsymbol{n})\, ds,$$

for any $v\in\mathcal{V}_k(P)$ and $\boldsymbol{p}\in[\mathcal{P}_{k-1}(P)]^d$.

We next describe the quadrature schemes that are used in the numerical studies. For the 2D case, we adopt a triangulation scheme that divides each polygonal element into triangles by connecting the centroid to each vertex and apply the Dunavant rules [131] in each subdivided triangle. According to the above-stated

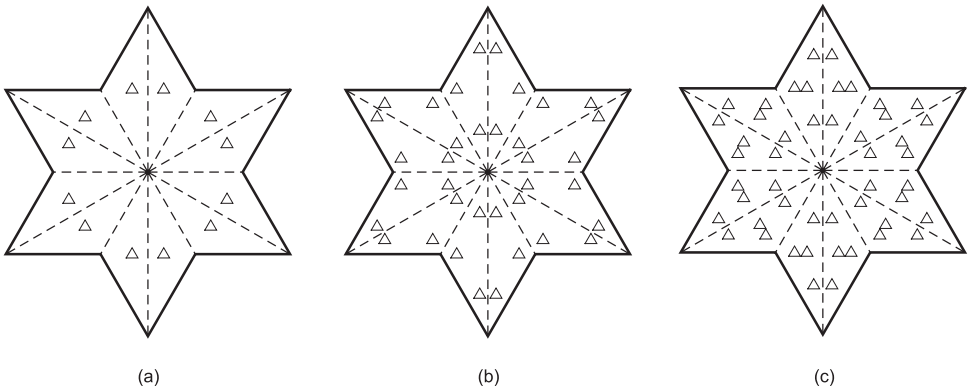

Figure 12.4 Illustration of the "triangulation" scheme for general polygons in the physical domain. (a) 1st order triangulation scheme, (b) 2nd order triangulation scheme, and (c) 3rd order triangulation scheme.

requirements, instead of using a one-point rule, the 1st order triangulation scheme with one integration point per subdivided triangle is used for linear elements to avoid spurious energy modes. For quadratic elements, the 2nd order triangulation scheme is employed, which contains three integration points per subdivided triangle. Furthermore, the 3rd order triangulation scheme is also used to investigate the effect of increasing integration orders on the accuracy of the results in the gradient correction scheme. Illustrations of these schemes are shown in Figure 12.4(a)–12.4(c). As a side note, the triangulation scheme requires polygonal elements to be star-convex with respect to their centroids, which is indeed the case for all the examples presented here. Other quadrature schemes can also be utilized in conjunction with the gradient correction scheme, such as those specifically designed for integrating polynomial functions over arbitrary polygonal domains [102, 285, 286], as long as they satisfy the requirements stated in this section.

For volumetric integration in the 3D case, one possibility is to split the element into tetrahedra and use the available quadrature schemes on these subdomains. A more economical alternative for the linear polyhedron that satisfies the polynomial precision requirement is proposed in [322] and utilized in [47, 393]. This scheme, which is illustrated in Figure 12.5, can exactly integrate constant and linear fields. Additional options are noted in [102], which is designed for general polyhedral domains.

Regarding the boundary quadrature, the one-dimensional Gauss–Lobatto quadrature rule is adopted in 2D, which uses two integration points per edge for linear elements and three integration points per edge for quadratic elements. As for the boundary quadrature in 3D, the integration on each face is carried out by means of a vertex quadrature rule that requires only the evaluation of the integrand at the vertices of the face. The face is split into quadrilateral regions associated with its vertices by connecting the centroid to the midpoint of the edges of the faces. The

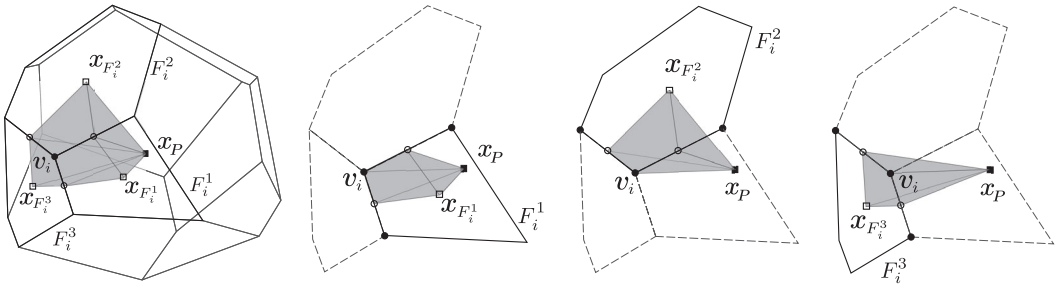

Figure 12.5 Illustration of the volumetric integration rule used for 3D linear polyhedrals. The weight associated with vertex $\boldsymbol{v}_i$ is the volume of the dark gray polyhedron formed by pyramids associated with the faces connected to $\boldsymbol{v}_i$. The pyramid associated with a face F_i^j is formed by the centroid of the element $\boldsymbol{x}_P$, centroid of the face $\boldsymbol{x}_{F_i^j}$, and the midpoint of the edges of F_i^j connected to $\boldsymbol{v}_i$. This figure is taken from [393].

quadrature weights are the areas of these quadrilateral regions. It can be shown that this scheme is exact for integration of linear fields (see Appendix of [268]).

12.5 GRADIENT CORRECTION SCHEME AND ITS PROPERTIES

In this section, the gradient correction scheme by Talischi et al. [393] is presented. First, we review the scheme for scalar problems and then show its extension to vectorial problems.

12.5.1 Gradient correction for scalar problems

Given an element P, the basic idea of the gradient correction scheme is to correct the gradient of functions in the local space $\mathcal{V}_k(P)$ with minimal perturbations that result in the satisfaction of a discrete divergence theorem. For scalar problems, the *corrected* gradient of $v \in \mathcal{V}_k(P)$, henceforth denoted by $\nabla_{P,k} v$, is taken to be a vector field over P that solves the optimization problem

$$\min_{\boldsymbol{\xi}} \fint_P \|\boldsymbol{\xi} - \nabla v\|^2 \, d\boldsymbol{x}, \tag{12.7}$$

subject to

$$\fint_P \boldsymbol{p} \cdot \boldsymbol{\xi} \, d\boldsymbol{x} = -\fint_P v \nabla \cdot \boldsymbol{p} \, d\boldsymbol{x} + \oint_{\partial P} v(\boldsymbol{p} \cdot \boldsymbol{n}) \, ds \quad \forall \boldsymbol{p} \in [\mathcal{P}_{k-1}(P)]^d. \tag{12.8}$$

The above constrained minimization is carried out over all sufficiently smooth vector fields on P such that the utilized quadrature makes sense. The corrected gradient

$$\nabla_{P,k} v = [(\nabla_{P,k} v)_x, (\nabla_{P,k} v)_y]^T \text{ in 2D}$$
$$\nabla_{P,k} v = [(\nabla_{P,k} v)_x, (\nabla_{P,k} v)_y, (\nabla_{P,k} v)_z]^T \text{ in 3D}$$

is thus the "closest"[†] field to $\nabla v = [(\nabla v)_x, (\nabla v)_y]^T$ (or $\nabla v = [(\nabla v)_x, (\nabla v)_y, (\nabla v)_z]^T$ in 3D) that satisfies the discrete divergence theorem against all polynomials of order k.

To assist the formal definition of the gradient correction scheme for scalar problems, we consider a basis $\{\boldsymbol{\zeta}_1, \ldots, \boldsymbol{\zeta}_n\}$ for $[\mathcal{P}_{k-1}(P)]^d$ and replace the equality constraint (12.8) by the equivalent set of constraints:

$$\fint_P \boldsymbol{\zeta}_a \cdot \boldsymbol{\xi}\, d\boldsymbol{x} = -\fint_P v \nabla \cdot \boldsymbol{\zeta}_a\, d\boldsymbol{x} + \oint_{\partial P} v(\boldsymbol{\zeta}_a \cdot \boldsymbol{n})\, ds, \quad a = 1, \ldots, n$$

Introducing multipliers $\lambda_1, \ldots, \lambda_n$, one obtains the Lagrangian:

$$\begin{aligned}\mathcal{L}(\boldsymbol{\xi}, \lambda_1, \ldots, \lambda_n) = &\fint_P \|\boldsymbol{\xi} - \nabla v\|^2\, d\boldsymbol{x} \\ &+ \sum_{a=1}^{n} \lambda_a \left[\fint_P \boldsymbol{\zeta}_a \cdot \boldsymbol{\xi}\, d\boldsymbol{x} + \fint_P v \nabla \cdot \boldsymbol{\zeta}_a\, d\boldsymbol{x} - \oint_{\partial P} v(\boldsymbol{\zeta}_a \cdot \boldsymbol{n})\, ds\right].\end{aligned}$$

The optimality of $\nabla_{P,k} v$ requires that for any variation $\boldsymbol{\eta}$,

$$D_{\boldsymbol{\xi}} \mathcal{L}(\nabla_{P,k} v, \lambda_1, \ldots, \lambda_n)[\boldsymbol{\eta}] = 2 \fint_P (\nabla_{P,k} v - \nabla v) \cdot \boldsymbol{\eta}\, d\boldsymbol{x} + \sum_{a=1}^{n} \lambda_a \fint_P \boldsymbol{\zeta}_a \cdot \boldsymbol{\eta}\, d\boldsymbol{x} = 0,$$

and therefore

$$\fint_P \left(\nabla_{P,k} v - \nabla v + \sum_{a=1}^{n} \frac{1}{2} \lambda_a \boldsymbol{\zeta}_a\right) \cdot \boldsymbol{\eta}\, d\boldsymbol{x} = 0.$$

This shows that the perturbation $\nabla_{P,k} v - \nabla v$ coincides with an element of $[\mathcal{P}_{k-1}(P)]^d$ at the location of the quadrature points, because the optimization problem (12.7)–(12.8) can only prescribe the values of $\nabla_{P,k} v$ at the quadrature points. Therefore, we can officially define the corrected gradient $\nabla_{P,k} v$ as the field satisfying the following two conditions:

- $\nabla_{P,k} v - \nabla v \in [\mathcal{P}_{k-1}(P)]^d$.
- For all $\boldsymbol{p} \in [\mathcal{P}_{k-1}(P)]^d$,

$$\fint_P \boldsymbol{p} \cdot \nabla_{P,k} v\, d\boldsymbol{x} = -\fint_P v \nabla \cdot \boldsymbol{p}\, d\boldsymbol{x} + \oint_{\partial P} v(\boldsymbol{p} \cdot \boldsymbol{n})\, ds. \tag{12.9}$$

We observe from these two conditions that $\nabla_{P,k}$ is a linear map, and so in practice only the action of $\nabla_{P,k}$ on the basis of $\mathcal{V}_k(P)$ must be computed. Here, we present the details on a systematic procedure for computing the corrected gradient of the basis functions for arbitrary k. We denote $\{\phi_1^{(k)}, \cdots, \phi_{n_\mathcal{V}}^{(k)}\}$ as the basis for $\mathcal{V}_k(P)$,

[†]The distance here is with respect to the quadrature form of the L^2-metric.

where $n\mathcal{V}$ is the dimension of the space $\mathcal{V}_k(P)$. Our goal is to find a coefficient matrix $\boldsymbol{S}$ such that

$$\nabla_{P,k}\phi_i^{(k)} = \nabla\phi_i^{(k)} + \sum_{a=1}^{n\mathcal{P}} S_{ia}\boldsymbol{\zeta}_a \quad \forall i = 1,\ldots,n\mathcal{V}.$$

To explicitly compute $\boldsymbol{S}$, we further define matrices $\boldsymbol{R}$ of size $n\mathcal{V}\times n\mathcal{P}$, and $\boldsymbol{M}$ of size $n\mathcal{P}\times n\mathcal{P}$ with the following forms:

$$R_{ia} = \oint_{\partial P}(\boldsymbol{\zeta}_a\cdot\boldsymbol{n})\phi_i^{(k)}\,ds - \fint_P \phi_i^{(k)}\nabla\cdot\boldsymbol{\zeta}_a\,d\boldsymbol{x} - \fint_P \boldsymbol{\zeta}_a\cdot\nabla\phi_i^{(k)}\,d\boldsymbol{x},$$

and

$$M_{ab} = \fint_{\partial P}\boldsymbol{\zeta}_a\cdot\boldsymbol{\zeta}_b\,d\boldsymbol{x}.$$

Replacing v and $\boldsymbol{p}$ with ϕ_i^k and $\boldsymbol{\zeta}_b$ in (12.9) yields the linear system of equations

$$\sum_{a=1}^{n\mathcal{P}} S_{ia}M_{ab} = R_{ib} \quad \forall i = 1,\ldots,n\mathcal{V} \qquad \text{and} \qquad b = 1,\ldots,n\mathcal{P}.$$

Therefore, the coefficient matrix is obtained as $\boldsymbol{S} = \boldsymbol{R}\boldsymbol{M}^{-1}$.

In order to better understand the gradient correction scheme, let us denote by $\boldsymbol{p}_v$ the perturbation to ∇v that gives the corrected gradients, that is,

$$\nabla_{P,k}v = \nabla v + \boldsymbol{p}_v.$$

Inserting the above in (12.9), we get for any $\boldsymbol{p}\in[\mathcal{P}_{k-1}(P)]^d$,

$$\fint_P \boldsymbol{p}\cdot\boldsymbol{p}_v\,d\boldsymbol{x} = \left[-\fint_P v\nabla\cdot\boldsymbol{p}\,d\boldsymbol{x} + \oint_{\partial P} v(\boldsymbol{p}\cdot\boldsymbol{n})ds\right] - \fint_P \boldsymbol{p}\cdot\nabla v\,d\boldsymbol{x}. \tag{12.10}$$

Several observations can be made. First, the integral on the left-hand side of the above equation is exactly computed by the utilized quadrature (recall that we require the quadrature to be exact for polynomial functions up to order $2k-2$). Second, notice the right-hand side of the above expression represents the difference of the two quadrature approximations (the two quadrature approximations are the terms in the bracket and the last term, respectively) of $\int_P \boldsymbol{p}\cdot\nabla v\,d\boldsymbol{x}$. Therefore, (12.10) shows that the perturbations $\boldsymbol{p}_v$ capture the difference between two approximations of ∇v when integrated against polynomials of order $k-1$. $\boldsymbol{p}_v$ is, in fact, the "smallest" element in $[\mathcal{P}_{k-1}(P)]^d$ with respect to the L^2-norm that does so according to (12.7)–(12.8). Third, the smaller the error in the satisfaction of the discrete divergence theorem $\big($i.e., right-hand side of (12.10)$\big)$, the smaller the perturbation is to the gradient. This error depends on the accuracy of quadrature as well as the nature of the functions in the local space $\mathcal{V}_k(P)$. Last but not least,

by setting $\boldsymbol{p} = \nabla_{P,k} q - \nabla q = \boldsymbol{p}_q$ in (12.10), we have

$$\begin{aligned}\int_P (\nabla_{P,k} q - \nabla q)^2 d\boldsymbol{x} &= -\fint_P q \nabla \cdot \boldsymbol{p}_q \, d\boldsymbol{x} + \oint_{\partial P} q(\boldsymbol{p}_q \cdot \boldsymbol{n}) \, ds - \fint_P \boldsymbol{p}_q \cdot \nabla q \, d\boldsymbol{x} \\ &= -\int_P q \nabla \cdot \boldsymbol{p}_q \, d\boldsymbol{x} + \int_{\partial P} q(\boldsymbol{p}_q \cdot \boldsymbol{n}) \, ds - \int_P \boldsymbol{p}_q \cdot \nabla q \, d\boldsymbol{x} \\ &= 0,\end{aligned}$$

which implies that the corrected gradient coincides with the exact gradient when applied to k-th order polynomials, i.e.,

$$\nabla_{P,k} q = \nabla q \quad \forall q \in \mathcal{P}_k(P). \tag{12.11}$$

This property of the correction scheme plays an important role in ensuring that the resulting discretizations are polynomially consistent and satisfy the patch test.

To aid in better understanding (12.11), we consider the case with linear space $\mathcal{V}_1(P)$, where an explicit expression for the corrected gradient can be readily obtained. Let $\boldsymbol{p} \in [\mathcal{P}_0(P)]^d$ and $v \in \mathcal{V}_1(P)$. We arrive at the following expression for the corrected gradient:

$$\nabla_{P,1} v = \nabla v + \frac{1}{|P|} \left(\oint_{\partial P} v \boldsymbol{n} \, ds - \fint_P \nabla v \, d\boldsymbol{x} \right),$$

which is similar to the corrected strain operator in the meshfree literature [296]. We can see from this expression that the perturbation is a constant field proportional to the error in satisfying the identity $\int_P \nabla v \, d\boldsymbol{x} = \int_{\partial P} v \boldsymbol{n} \, ds$ by the volumetric and surface quadrature schemes. This implies that if $v \in \mathcal{P}_1(P)$, then there is no correction to its gradient, i.e., $\nabla_{P,1} v = \nabla v$. Additionally, in the 2D case, recall that the variation of v on ∂P is piecewise linear, and the boundary quadrature is exact. In this case, $\oint_{\partial P} v \boldsymbol{n} \, ds = \int_{\partial P} v \boldsymbol{n} \, ds = \int_P \nabla v \, d\boldsymbol{x}$, and subsequently

$$\nabla_{P,1} v = \nabla v + \frac{1}{|P|} \left(\int_P \nabla v \, d\boldsymbol{x} - \fint_P \nabla v \, d\boldsymbol{x} \right). \tag{12.12}$$

The perturbation is simply the difference between the volume average of ∇v and its approximations through the quadrature. An immediate observation from (12.12) is that

$$\fint_P \nabla_{P,1} v \, d\boldsymbol{x} = \int_P \nabla v \, d\boldsymbol{x}.$$

This shows that the corrected gradient $\nabla_{P,1} v$ under the action of the quadrature behaves like ∇v under exact integration.

Generally, it is expected from the definition of the correction that

$$\fint_P \boldsymbol{\psi} \cdot \nabla_{P,k} v \, d\boldsymbol{x} - \int_P \boldsymbol{\psi} \cdot \nabla v \, d\boldsymbol{x} = O(h_P^k) \|\nabla v\|_{L^2(P)^d}$$

for $v \in \mathcal{V}_k(P)$ when $\boldsymbol{\psi}$ is a sufficiently smooth vector field. Here, h_P is the diameter of element P.

12.5.2 Gradient correction for vectorial problems

The gradient correction scheme defined in the preceding subsection for scalar problems can be readily extended to vectorial problems. For a vector field $\boldsymbol{v} = [v_x, v_y]^T$ (or $\boldsymbol{v} = [v_x, v_y, v_z]^T$ in 3D) $\in [\mathcal{V}_k(P)]^d$, the gradient correction scheme takes the form

$$\nabla_{P,k} \otimes \boldsymbol{v} = \begin{bmatrix} (\nabla_{P,k} v_x)^T \\ (\nabla_{P,k} v_y)^T \end{bmatrix} \text{ in 2D}, \quad \nabla_{P,k} \otimes \boldsymbol{v} = \begin{bmatrix} (\nabla_{P,k} v_x)^T \\ (\nabla_{P,k} v_y)^T \\ (\nabla_{P,k} v_z)^T \end{bmatrix} \text{ in 3D}.$$

Similar to the scalar case, the corrected gradient satisfies the discrete divergence theorem,

$$\fint_P \boldsymbol{p} : \nabla_{P,k} \otimes \boldsymbol{v} \, d\boldsymbol{x} = \int_{\partial E} (\boldsymbol{p} \cdot \boldsymbol{n}) \cdot \boldsymbol{v} \, ds - \fint_P \boldsymbol{v} \cdot (\nabla \cdot \boldsymbol{p}) \, d\boldsymbol{x} \quad \forall \, \boldsymbol{p} \in [\mathcal{P}_{k-1}(P)]^{d \times d},$$

and, moreover, for any sufficiently smooth second-order tensorial field $\boldsymbol{\psi}$, the element-level consistency error satisfies

$$\fint_P \boldsymbol{\psi} : \nabla_{P,k} \otimes \boldsymbol{v} \, d\boldsymbol{x} - \int_P \boldsymbol{\psi} : \nabla \boldsymbol{v} \, d\boldsymbol{x} = \mathcal{O}(h_P^k) \|\nabla \boldsymbol{v}\|_{L^2(P)^d}.$$

In the computational implementation of 2D problems, let us assume the set of basis functions $\{\boldsymbol{\phi}_1^{(k)}, \ldots, \boldsymbol{\phi}_{2n\mathcal{V}}^{(k)}\}$ of $\left[\mathcal{V}_k(P)\right]^2$ are of the form

$$\boldsymbol{\phi}_{2i-1}^{(k)} = \left[\phi_i^{(k)}, 0\right]^T, \quad \boldsymbol{\phi}_{2i}^{(k)} = \left[0, \phi_i^{(k)}\right]^T$$

for $i = 1, \ldots, n\mathcal{V}$, and where $n\mathcal{V}$ is the dimension of the space $\mathcal{V}_k(P)$. The correction scheme for vectorial problems in practice amounts to correcting each basis function as follows:

$$\nabla_{P,k} \otimes \boldsymbol{\phi}_{2i-1}^{(k)} = \begin{bmatrix} \left(\nabla_{P,k} \phi_i^{(k)}\right)^T \\ \mathbf{0} \end{bmatrix}, \quad \nabla_{P,k} \otimes \boldsymbol{\phi}_{2i}^{(k)} = \begin{bmatrix} \mathbf{0} \\ \left(\nabla_{P,k} \phi_i^{(k)}\right)^T \end{bmatrix}$$

for $i = 1, \ldots, n\mathcal{V}$, and where $\nabla_{P,k} \phi_i^{(k)}$ is the computed corrected gradient of the shape function according to the procedure outlined for the scalar problem.

Similarly, let us assume the set of basis functions for $\{\boldsymbol{\phi}_1^{(k)}, \ldots, \boldsymbol{\phi}_{3n\mathcal{V}}^{(k)}\}$ of the 3D space $\left[\mathcal{V}_k(P)\right]^3$ are of the form

$$\boldsymbol{\phi}_{3i-3}^{(k)} = \left[\phi_i^{(k)}, 0, 0\right]^T, \quad \boldsymbol{\phi}_{3i-1}^{(k)} = \left[0, \phi_i^{(k)}, 0\right]^T, \quad \text{and} \quad \boldsymbol{\phi}_{3i}^{(k)} = \left[0, 0, \phi_i^{(k)}\right]^T$$

for $i = 1, \ldots, n\mathcal{V}$. The gradient correction scheme for 3D vectorial problems corrects each basis function as

$$\nabla_{P,k} \otimes \boldsymbol{\phi}_{3i-2}^{(k)} = \begin{bmatrix} \left(\nabla_{P,k} \phi_i^{(k)}\right)^T \\ \mathbf{0} \\ \mathbf{0} \end{bmatrix}, \quad \nabla_{P,k} \otimes \boldsymbol{\phi}_{3i-1}^{(k)} = \begin{bmatrix} \mathbf{0} \\ \left(\nabla_{P,k} \phi_i^{(k)}\right)^T \\ \mathbf{0} \end{bmatrix},$$

$$\nabla_{P,k} \otimes \boldsymbol{\phi}_{3i}^{(k)} = \begin{bmatrix} \mathbf{0} \\ \mathbf{0} \\ \left(\nabla_{P,k} \phi_i^{(k)}\right)^T \end{bmatrix} \quad (i = 1, \ldots, n\mathcal{V}).$$

12.6 CONFORMING GALERKIN APPROXIMATIONS

Consider Ω_h to be a finite element decomposition of the domain Ω into non-overlapping polygons or polyhedra, where h is the average element size. The boundary of the mesh, denoted as Γ_h, is assumed to be compatible with the applied boundary condition. In other words, $\Gamma_h^{\boldsymbol{t}}$ and $\Gamma_h^{\boldsymbol{x}}$ are both unions of edges of the mesh.

We define the numerical integration $\fint_{\Omega_h}$ on Ω_h as the summation of the contributions from numerical integrals $\fint_P$ from each element P following the standard assembly rule, namely, $\fint_{\Omega_h} = \sum_{P\in\Omega_h} \fint_P$, and $\oint_{\Gamma_h^{\boldsymbol{t}}}$ as the numerical integration on $\Gamma_h^{\boldsymbol{t}}$. Similarly, we define the gradient correction map on the global level, $\nabla_{h,k}\colon \mathcal{K}_{h,k} \to [L^2(\Omega_h)]^{d\times d}$, such that it coincides with the gradient correction map $\nabla_{P,k}$ at the element level,

$$(\nabla_{h,k}\boldsymbol{v}_h)|_P = \nabla_{P,k} \otimes (\boldsymbol{v}_h|_P) \quad \forall P \in \Omega_h \qquad \text{and} \qquad \boldsymbol{v}_h \in \mathcal{K}_{h,k}.$$

The Galerkin approximation of the displacement-based formulation then consists of finding $\boldsymbol{u}_h \in \mathcal{K}_{h,k}$, such that

$$G_h(\boldsymbol{u}_h, \delta\boldsymbol{v}_h) = 0 \quad \forall \delta\boldsymbol{v}_h \in \mathcal{K}^0_{h,k},$$

where $\mathcal{K}^0_{h,k} = \mathcal{K}_{h,k} \bigcap \mathcal{K}^0$ and $G_h(\boldsymbol{u}_h, \delta\boldsymbol{v}_h)$ is the discretization and quadrature evaluation of $G(\boldsymbol{u}, \delta\boldsymbol{v})$ in (12.3) with the exact gradient operator ∇ replaced by $\nabla_{h,k}$, which takes the form

$$G_h(\boldsymbol{u}_h, \delta\boldsymbol{v}_h) = \fint_{\Omega_h} \frac{\partial W}{\partial \boldsymbol{F}}(\boldsymbol{x}, \boldsymbol{I} + \nabla_{h,k}\boldsymbol{u}_h) : \nabla_{h,k}(\delta\boldsymbol{v}_h)\, d\boldsymbol{x} - \fint_{\Omega_h} \boldsymbol{f}_h \cdot \delta\boldsymbol{v}_h\, d\boldsymbol{x} - \oint_{\Gamma_h^{\boldsymbol{t}}} \boldsymbol{t}_h \cdot \delta\boldsymbol{v}_h\, ds, \quad (12.13)$$

and terms $\boldsymbol{f}_h$ and $\boldsymbol{t}_h$ are the approximated body force and boundary traction, respectively.

For the two-field mixed formulation, if we introduce the additional finite element space $\mathcal{Q}^D_{h,k-1}$(or $\mathcal{Q}^C_{h,k-1}$)$\subseteq \mathcal{Q}$, the Galerkin approximation consists of finding $(\boldsymbol{u}_h, \widehat{p}_h) \in \mathcal{K}_{h,k} \times \mathcal{Q}^D_{h,k-1}$(or $\mathcal{Q}^C_{h,k-1}$), such that

$$\begin{aligned} G_h^{\boldsymbol{v}}(\boldsymbol{u}_h, \widehat{p}_h, \delta\boldsymbol{v}_h) &= 0 \quad \forall \delta\boldsymbol{v}_h \in \mathcal{K}^0_{h,k}, \\ G_h^{\widehat{q}}(\boldsymbol{u}_h, \widehat{p}_h, \delta\widehat{q}_h) &= 0 \quad \forall \delta\widehat{q}_h \in \mathcal{Q}^D_{h,k-1} \quad (\text{or } \mathcal{Q}^C_{h,k-1}), \end{aligned}$$

with $G_h^{\boldsymbol{v}}(\boldsymbol{u}_h, \widehat{p}_h, \delta\boldsymbol{v}_h)$ and $G_h^{\widehat{q}}(\boldsymbol{u}_h, \widehat{p}_h, \delta\widehat{q}_h)$ being of the form

$$G_h^{\boldsymbol{v}}(\boldsymbol{u}_h, \widehat{p}_h, \delta\boldsymbol{v}_h) = \fint_{\Omega_h} \left[-\frac{\partial \widehat{W}^*}{\partial \boldsymbol{F}}(\boldsymbol{x}, \boldsymbol{I} + \nabla_{h,k}\boldsymbol{u}_h, \widehat{p}_h) + \widehat{p}_h \operatorname{adj}\big(\boldsymbol{I} + (\nabla_{h,k}\boldsymbol{u}_h)^T\big) \right] : \nabla_{h,k}(\delta\boldsymbol{v}_h)\, d\boldsymbol{x} - \fint_{\Omega_h} \boldsymbol{f}_h \cdot \delta\boldsymbol{v}_h\, d\boldsymbol{x} - \oint_{\Gamma_h^{\boldsymbol{t}}} \boldsymbol{t}_h \cdot \delta\boldsymbol{v}_h\, ds, \quad (12.14)$$

$$G_h^{\widehat{q}}(\boldsymbol{u}_h, \widehat{p}_h, \delta\widehat{q}_h) = \fint_{\Omega_h} \left[\det(\boldsymbol{I} + \nabla_{h,k}\boldsymbol{u}_h) - 1 - \frac{\partial \widehat{W}^*}{\partial \widehat{p}}(\boldsymbol{x}, \boldsymbol{I} + \nabla_{h,k}\boldsymbol{u}_h, \widehat{p}_h) \right] \delta\widehat{q}_h \, d\boldsymbol{x}. \tag{12.15}$$

Notice that since we replace the gradient operators ∇ in both $\boldsymbol{u}_h$ and $\delta\boldsymbol{v}_h$ in (12.13), (12.14), and (12.15) with $\nabla_{h,k}$, the resulting approximations yield symmetric linearizations. Moreover, both of the above finite element approximations pass the first-order patch test [100]. This means that when the exact displacement field is a linear field, the above finite element approximations give the exact results.

12.7 NUMERICAL EXAMPLES

In this section, we present a series of numerical tests to assess the performance of the displacement-based and the two-field mixed polygonal and polyhedral finite element methods. For 2D problems, both displacement-based and mixed polygonal elements up to the second order are considered, whereas only first-order displacement-based polyhedral elements are studied for the 3D case. We demonstrate, through the convergence studies of two boundary-value problems, that the gradient correction scheme is capable of ensuring optimal convergence of polygonal and polyhedral elements in finite elasticity. For mixed polygonal elements, we also provide numerical evaluations and discuss inf-sup stability for different choices of pressure approximations.

Throughout this section, a neo-Hookean material model is considered. For a compressible neo-Hookean material, the stored-energy function characterizing the material behavior has the form

$$W(\boldsymbol{F}) = \frac{\mu}{2}[\boldsymbol{F} : \boldsymbol{F} - 3] - \mu(\det \boldsymbol{F} - 1) + \frac{3\kappa + \mu}{6}(\det \boldsymbol{F} - 1)^2,$$

where μ and κ denote the initial shear and bulk moduli of the material response. In the limit of incompressibility ($\kappa \to \infty$), the above compressible neo-Hookean material reduces to the standard neo-Hookean stored-energy function

$$W(\boldsymbol{x}, \boldsymbol{F}) = \begin{cases} \dfrac{\mu}{2}[\boldsymbol{F} : \boldsymbol{F} - 3], & \text{if } \det \boldsymbol{F} = 1, \\ +\infty, & \text{otherwise.} \end{cases} \tag{12.16}$$

The standard Newton–Raphson method is employed to solve the nonlinear system of equations, and we assume that convergence at each loading step is met if the norm of the residual falls below 10^{-8} times that of the initial residual.

12.7.1 Displacement-based polygonal and polyhedral elements

This subsection presents a convergence study of the displacement-based polygonal and polyhedral finite elements using the gradient correction scheme. In particular, we consider a boundary-value problem as shown in Figure 12.6(a), where a rectangular block of dimensions $1 \times 1 \times \pi$ is bent into a semi-circular shape. The corresponding analytical displacement solution $\boldsymbol{u}$ is given by

$$u_x = -1 + (1 + x)\cos(z) - x, \qquad u_y = 0, \qquad u_z = (1 + x)\sin(z) - z,$$

while the corresponding body force $\boldsymbol{f} = [f_x, f_y, f_z]^T$ reads as

$$f_x = -\frac{(1+x)\cos(z)(3\kappa - 2\mu)}{3}, \qquad f_y = 0, \qquad f_z = -\frac{(1+x)\sin(z)(3\kappa - 2\mu)}{3}.$$

Throughout, we set the initial shear and bulk moduli μ and κ as 1 and 10, and consider two error measures, the L^2-norm and the H^1-seminorm of the displacement error. More specifically, the L^2-norm and the H^1-seminorm, respectively, are given by

$$E_{0,\boldsymbol{u}} = \|\boldsymbol{u} - \boldsymbol{u}_h\| \qquad \text{and} \qquad E_{1,\boldsymbol{u}} = \|\nabla \boldsymbol{u} - \nabla \boldsymbol{u}_h\|,$$

where the L^2-norm, $\|\cdot\|$, is evaluated using a fifth order triangulation rule.

Since no deformation occurs in the u_y direction, this problem can be simplified into a plane strain problem as shown in Figure 12.6(b). We make use of structured

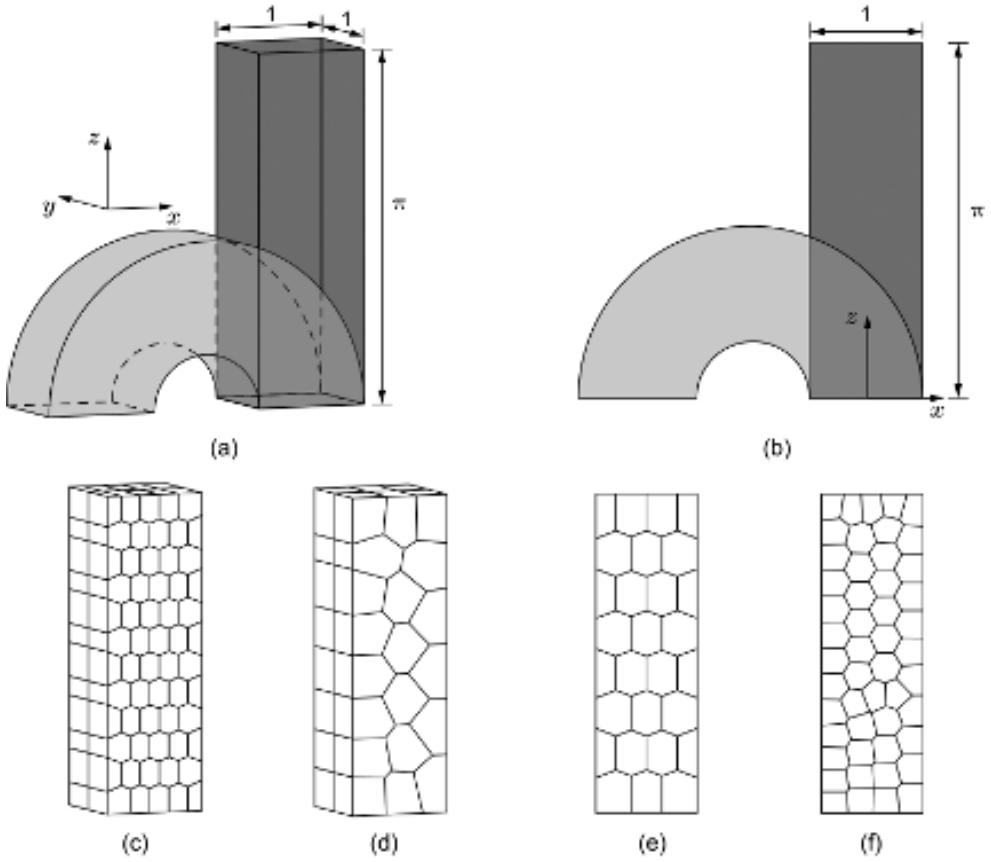

Figure 12.6 (a) An illustration of the 3D boundary-value problem. (b) Associated simplified 2D plane strain problem of (a). (c) An example of the extruded structured hexagonal mesh consists of 120 elements. (d) An example of the extruded CVT mesh with 40 elements. (e) An example of the 2D structured hexagonal mesh with 28 elements. (f) An example of the 2D CVT mesh with 50 elements.

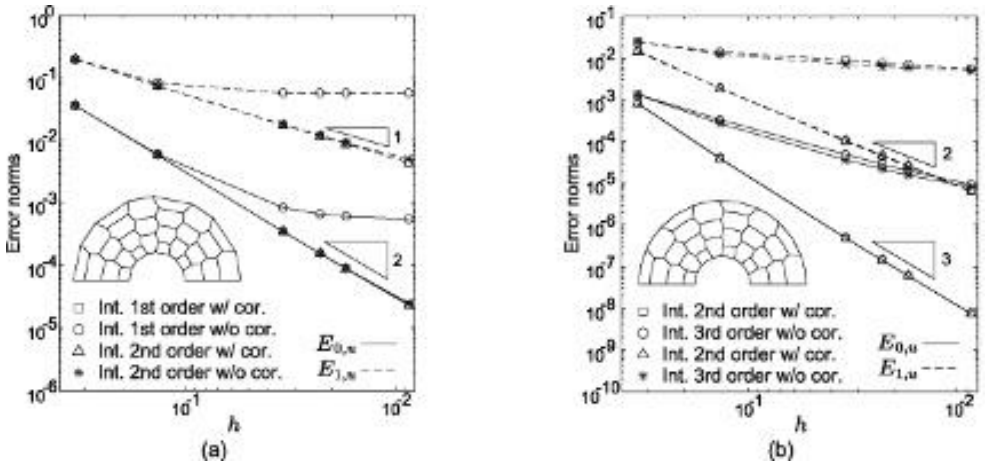

Figure 12.7 Plots of the error norms against the average mesh size h for structured hexagonal meshes with (a) linear polygonal elements and (b) quadratic polygonal elements.

hexagonal meshes to discretize the domain, an example of which is displayed in Figure 12.6(e). Both linear and quadratic polygonal elements are considered, which utilize the triangulation scheme with their required minimal order of accuracy (1st order for linear elements and 2nd order for quadratic element). To investigate the effect of increasing the integration order on the convergence and accuracy of the results, we also consider triangulation rules that are one order higher than the required minimum (2nd and 3rd orders for linear and quadratic elements, respectively). The results of the convergence study are summarized in Figure 12.7(a) and 12.7(b), respectively, for linear and quadratic polygonal elements. For linear polygonal elements, it is clear from the figure that, without the gradient correction, the 1st triangulation itself is not sufficient to ensure optimal convergence. However, the 2nd order triangulation rule seems sufficient to ensure sufficient accuracy and optimal convergence for the range of mesh sizes considered, even without the gradient correction scheme. We should note, however, that with further refinement of the mesh, we expect the consistency error to become dominant and the convergence rate to decrease. In contrast, for quadratic elements, both 2nd and 3rd order triangulation rules are not sufficient to ensure the optimal convergence of the finite element results without the gradient correction scheme.

When the gradient correction scheme is applied, the optimal convergence in the finite element results is recovered for both linear and quadratic polygonal elements with the triangulation schemes of minimal required orders. We also observe that the gradient correction scheme allows the use of the minimal required order of integration to achieve the same level of accuracy as with higher order integrations. If the gradient correction scheme is used, the displacement errors are identical for 1st and 2nd order triangulation rules for the linear polygonal elements and for 2nd and 3rd triangulation rules for the quadratic polygonal elements. This indicates

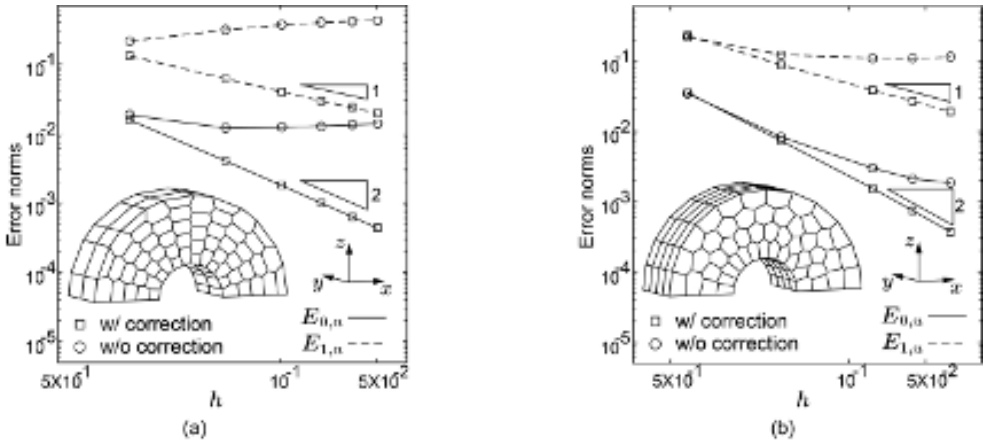

Figure 12.8 Plots of the error norms against the average mesh size h for (a) extruded structured hexagonal meshes and (b) extruded CVT meshes.

that the gradient corrections scheme can allow for a more efficient finite element implementation without sacrificing accuracy.

We also assess convergence for displacement-based polyhedral computations. To this end, we take the original 3D problem shown in Figure 12.6(a) and consider two types of polyhedral meshes, extruded structured hexagonal meshes and extruded centroid Voronoi tessellation (CVT) meshes, as shown in Figures 12.6(c) and 12.6(d), respectively. The convergence results for the displacement error norms as functions of the average mesh size are depicted in Figure 12.8. Each data point for the extruded CVT meshes is the mean of a five-mesh set. Again, the preliminary study indicates that the gradient correction scheme can ensure the optimal convergence for polyhedral elements.

12.7.2 Two-field mixed polygonal elements

In this subsection, together with the gradient correction scheme, the performance of mixed polygonal elements on inf-sup stability and convergence are numerically evaluated for the 2D case. In addition to the displacement error norms considered in the previous subsection, we define the L^2-norm of the pressure error

$$E_{0,\widehat{p}} = \|\widehat{p}_h - \widehat{p}\|,$$

which is evaluated using a fifth order quadrature scheme.

Inf-sup stability of polygonal discretizations

The satisfaction of the inf-sup stability condition is crucial to guarantee the convergence of mixed finite elements [58, 235, 293]. For finite elasticity problems, inf-sup stability is formally defined by the generalized inf-sup condition [235, 293], which

states that a strictly positive and size-independent constant C_0 exists such that

$$\beta_h(\boldsymbol{u}_h) = \inf_{\widehat{q}_h \in \mathcal{Q}_{h,k-1}^{D \text{ or } C}} \sup_{\boldsymbol{v}_h \in \mathcal{K}_{h,k}} \frac{\int_\Omega \widehat{q}_h \operatorname{adj}\big(I + (\nabla \boldsymbol{u}_h)^T\big) : \nabla \boldsymbol{v}_h \, d\boldsymbol{x}}{\|\nabla \boldsymbol{v}_h\| \, \|\widehat{q}_h\|} \geq C_0. \tag{12.17}$$

for any admissible displacement field $\boldsymbol{u}_h \in \mathcal{K}_{h,k}$. Because the above generalized inf-sup condition is deformation dependent and difficult to verify, we only consider the inf-sup condition in the linear elasticity context,

$$\beta_h^0 = \inf_{\widehat{q}_h \in \mathcal{Q}_{h,k-1}^{D \text{ or } C}} \sup_{\boldsymbol{v}_h \in \mathcal{K}_{h,k}} \frac{\int_\Omega \widehat{q}_h \nabla \cdot \boldsymbol{v}_h \, d\boldsymbol{x}}{\|\nabla \boldsymbol{v}_h\| \, \|\widehat{q}_h\|} \geq C_0, \tag{12.18}$$

which essentially is a special case of (12.17) when $\boldsymbol{u}_h = 0$. This example focuses on the inf-sup stability of polygonal discretizations in 2D (similar to Figure 12.6(b)). It is well known that most of the lower order standard mixed finite elements in 2D are not inf-sup stable, whereas Beirão da Veiga et al. [30] have derived a geometrical condition to guarantee the satisfaction of (12.18), if every internal vertex node in the mesh is connected to no more than three edges. However, the analogous condition for polygonal discretizations with higher order mixed polygonal elements is still unknown. For 3D problems, even with lower order displacement and piecewise-constant pressure polyhedral elements, the inf-sup stability of polyhedral meshes is still an open question and needs further investigation. Here, we adopt the so called inf-sup test [88] to numerically evaluate the inf-sup stability of the linear and quadratic polygonal elements on several polygonal discretizations. We remark that while passing the inf-sup test only constitutes a necessary condition for the satisfaction of the inf-sup condition, the inf-sup test has been shown to reliably predict the stability properties of many well-known mixed finite elements [88, 391]. We consider a unit square domain with imposed boundary conditions as shown in Figure 12.9(a) and consider three Voronoi-type discretizations: structured hexagonal meshes, CVT meshes, and random Voronoi meshes, examples of which are provided in Figure 12.9(b)–(d). In general, the Voronoi-type discretizations with lower order elements satisfy the geometrical condition of Beirão da Veiga et al. [30], except for several limiting special cases such as the one where the Voronoi seeds are aligned in a Cartesian grid, forming a Cartesian mesh. In the inf-sup test, we compute the stability index β_h^0 as a function of the average mesh size h for all the families of discretizations considered in Figure 12.9(e)–(g). Each point for the CVT and random Voronoi meshes represents an average from five results. The figures indicate that all three polygonal discretizations are inf-sup stable with both discontinuous and continuous pressure approximations, at least in the linear elasticity regime. In comparison, while the standard linear and quadratic mixed elements with continuous pressure approximations (the T–H family) are unconditionally stable [58], most of those with discontinuous pressure approximations (the C-R family), such as lower-order mixed triangular and quadrilateral elements, are inf-sup unstable [58, 88, 204].

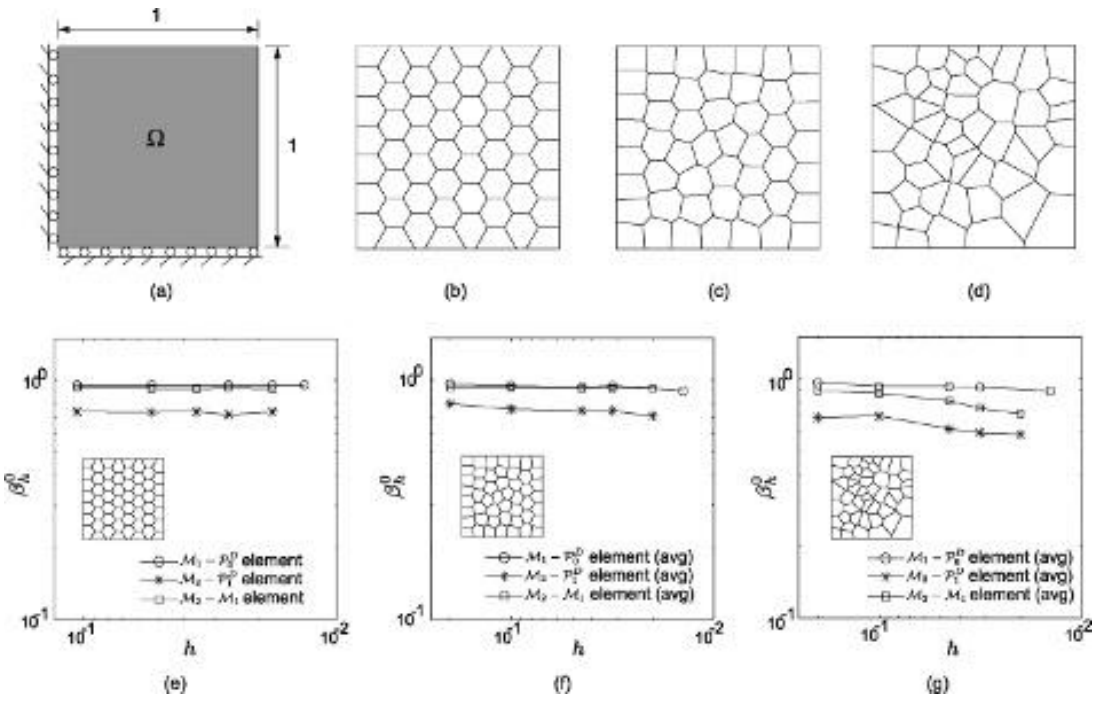

Figure 12.9 (a) Dimensions and boundary conditions adopted for the inf-sup test. (b) An example of the structured hexagonal dominant mesh with 56 elements. (c) An example of the randomly generated CVT mesh with 50 elements. (d) An example of the random Voronoi mesh with 50 elements. (e) Plot of the computed value of the stability index as a function of the average mesh size h for structured hexagonal dominant meshes. (f) Plot of the computed value of the stability index as a function of the average mesh size h for CVT meshes. (g) Plot of the computed value of the stability index as a function of the average mesh size h for random Voronoi meshes. This figure is adapted from [100].

Convergence study

Next we perform a convergence study of the two-field mixed elements through a 2D boundary-value problem, where an incompressible rectangular block with dimensions 1×1 is bent into a semicircle, as illustrated by Figure 12.6(b). The closed-form displacement and pressure solutions for such a problem read as

$$u_x = -r(-0.5) + r(x)\cos(y) - 0.5 - x, \qquad u_y = r(x)\sin(y) - y,$$

and

$$\widehat{p} = \frac{2\mu(4x^2 - 3)x - \sqrt{2}}{8x^2 - 4},$$

where the function $r(x)$ is given by $r(x) = \sqrt{2x + \sqrt{2}}$. In order to avoid the development of surface instabilities [44] and guarantee the uniqueness of the finite element solutions, the displacement boundary condition is prescribed on the left side of the block as well as the top and bottom of the block, leaving the right side of the block traction-free. Unlike in the previous subsection, we consider a family of CVT meshes, an example of which is shown in Figure 12.6(f), and plot the convergence results in Figure 12.10(a)–(f) for all three types of mixed polygonal finite elements. Each data point in the figures represents an average of the results from five meshes. We observe that optimal convergence in both displacement field and pressure field is recovered for both linear and quadratic mixed polygonal finite elements when the gradient correction scheme is adopted, as opposed to the case when no gradient correction scheme is used. Again, an identical level of accuracy in both the displacement and pressure fields is achieved with minimal and higher-order triangulation rules.

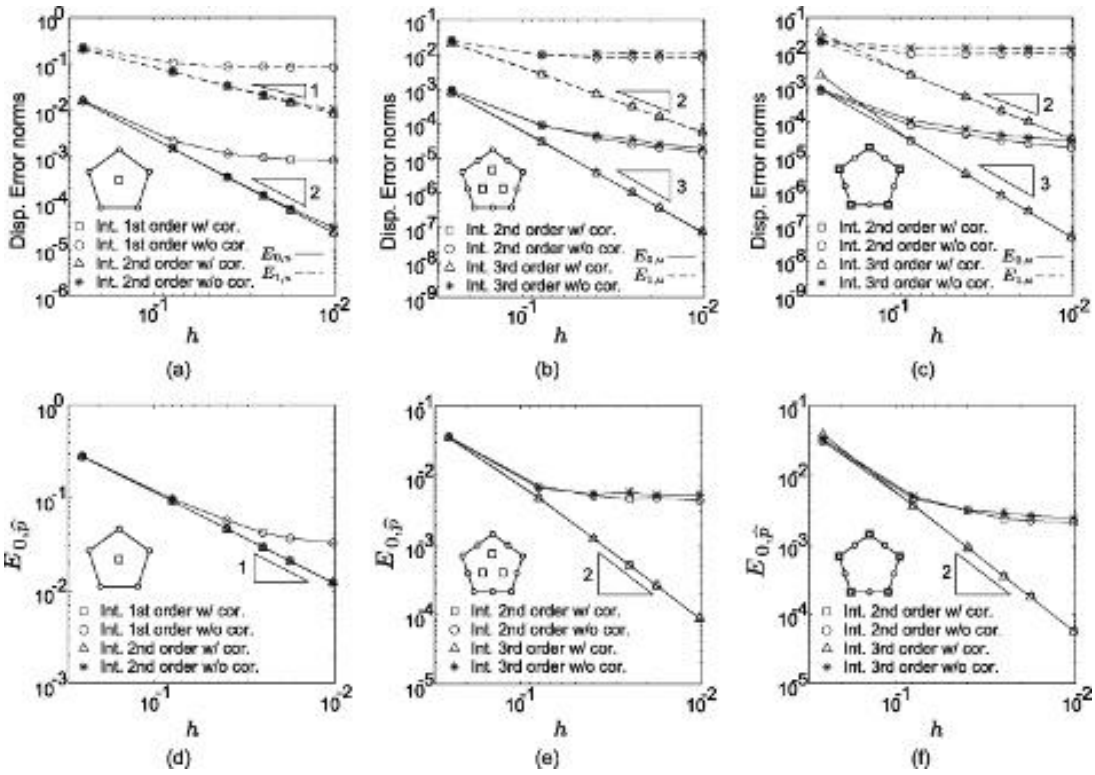

Figure 12.10 The displacement errors for the CVT meshes with (a) $\mathcal{M}_1 - \mathcal{P}_0^D$ elements, (b) $\mathcal{M}_2 - \mathcal{P}_1^D$ elements, and (c) $\mathcal{M}_2 - \mathcal{M}_1$ elements. The pressure errors for the CVT meshes with (d) $\mathcal{M}_1 - \mathcal{P}_0^D$ elements, (e) $\mathcal{M}_2 - \mathcal{P}_1^D$ elements, and (f) $\mathcal{M}_2 - \mathcal{M}_1$ elements.

12.8 APPLICATION TO THE STUDY OF FILLED ELASTOMERS

Experiments have demonstrated that typical filled elastomers contain stiff "interphases" or layers of stiff "bound rubber" around their inclusions [236]. The presence of such interphasial regions can significantly affect the macroscopic response of the filled elastomer when the fillers are submicron in size [175, 260]. In this section, the nonlinear elastic response of an incompressible elastomer reinforced with a random, isotropic distribution of circular rigid particles, bounded through finite-size interphases, is studied by means of polygonal finite elements. We aim at demonstrating the ability of polygonal finite elements to model the complex behavior of nonlinear elastic materials with extremely large localized deformations. Throughout this section, we consider each particle to be infinitely rigid and model them with the variational formulation proposed by Chi et al. [98]. This variational formulation treats the presence of each particle as a set of kinematic constraints on the displacement DOFs.

We approximate the truly random and isotropic distribution of particles by the periodic repetition of a unit cell in the $\boldsymbol{e}_1$ and $\boldsymbol{e}_2$ directions. The unit cell contains a total of 50 monodisperse rigid particles at an area fraction of $c_p = 25\%$. Each particle is bounded to the matrix by an interphase that is ten times stiffer than the matrix and whose thickness is assumed to be 20% of the radius of the particle, resulting in a total area fraction of $c_i = 11\%$. The mixed $\overline{\boldsymbol{F}}$-formulation is employed in this example and polygonal meshes with both linear and quadratic mixed elements are considered as shown in Figure 12.11(c) and (d). For comparison purposes, a finite element mesh with the commonly used 6-node hybrid quadratic triangular elements (termed CPE6MH) is included, as depicted in Figure 12.11(b). In order to make a fair comparison, all the meshes are generated such that they have a similar number of nodes in the matrix phase.

In the following study, we consider periodic boundary conditions [100, 260] for two loading conditions: (i) pure shear with average deformation gradient $\langle \boldsymbol{F} \rangle = \lambda \boldsymbol{e}_1 \otimes \boldsymbol{e}_1 + \lambda^{-1} \boldsymbol{e}_2 \otimes \boldsymbol{e}_2$ and (ii) simple shear with $\langle \boldsymbol{F} \rangle = \boldsymbol{I} + \gamma \boldsymbol{e}_1 \otimes \boldsymbol{e}_2$ where $\lambda \geq 1$ and $\gamma \geq 0$ denote the applied stretch and amount of shear, respectively. We remark that the periodicity in the pressure field cannot in general be enforced when employing mixed finite elements. At any rate, even when we use the T–H mixed elements where the pressure field is continuous, as shown in [100], the enforcement of periodic pressure boundary conditions only exerts a negligible influence on the solution. Moreover, the discontinuities of shear moduli between the matrix, interphase, and inclusions generate a discontinuous pressure field, which, in general, cannot be captured by mixed elements with continuous approximations for the pressure field, i.e., T–H elements. However, [100] has shown that using T-H elements (with minor levels of discontinuities (e.g., $\mu_i = 10\mu_m$) between the matrix and interphase) can still produce sufficiently accurate solutions, provided that the stiff inclusions are treated independently using the rigid-body constraint formulation by Chi et al. [98].

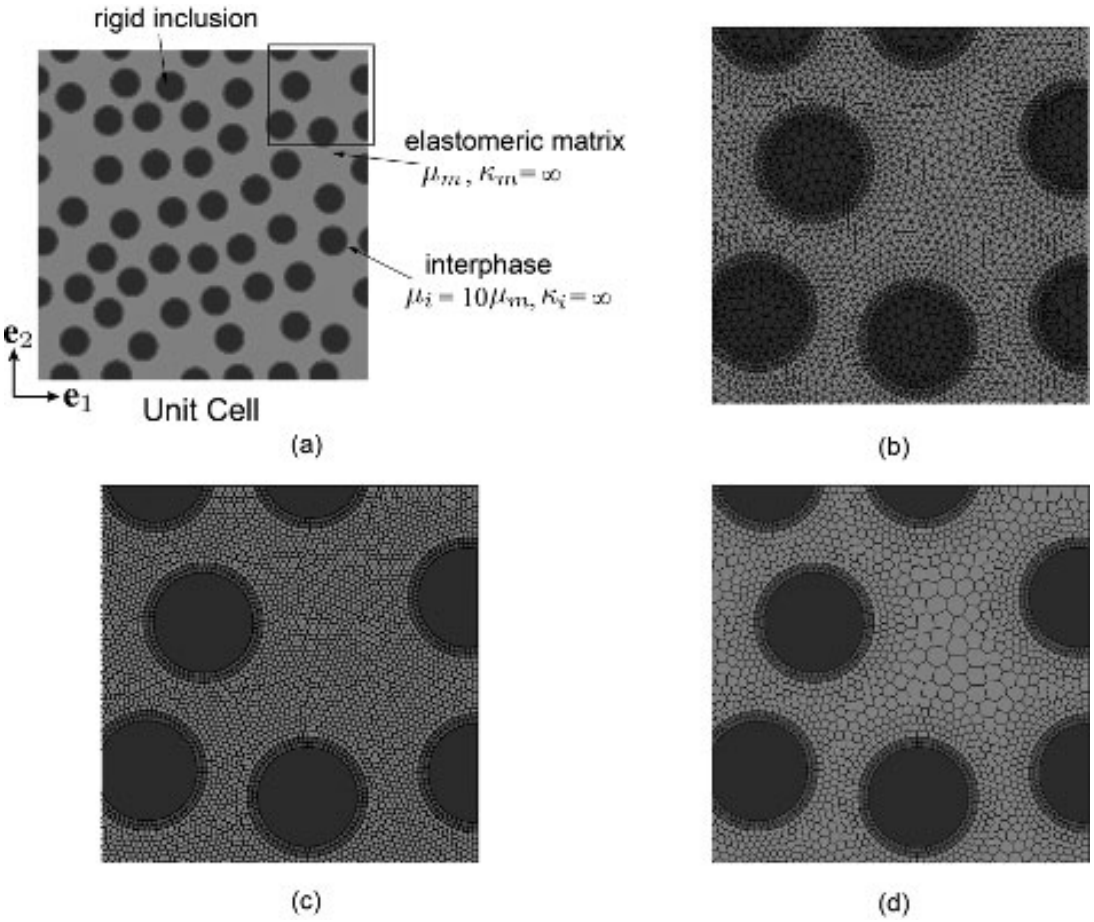

Figure 12.11 (a) The unit cell considered in the problem. (b) The quadratic triangular mesh comprised of 58,814 CPE6MH elements and 118,141 nodes in total, with 71,179 nodes in the matrix phase. (c) The linear polygonal mesh comprised of 39,738 elements and 76,020 nodes in total, with 66,095 nodes in the matrix phase. (d) The quadratic polygonal mesh comprised of 20,205 elements and 95,233 nodes in total, with 67,325 nodes in the matrix phase. This figure is adapted from [100]. See color insert.

12.8.1 Results for filled neo-Hookean elastomers

In this subsection, the matrix is assumed to be an incompressible neo-Hookean material, described by the stored-energy function (12.16). The initial shear modulus μ_m of the matrix is taken to be $\mu_m = 1$ MPa, and that of the interphase is set as $\mu_i = 10\,\mu_m = 10$ MPa. Figure 12.12(a)–(d) plots the deformed configurations of the unit cell obtained by $\mathcal{M}_2 - \mathcal{M}_1$, $\mathcal{M}_2 - \mathcal{P}_1^D$, $\mathcal{M}_1 - \mathcal{P}_0^D$, and CPE6MH elements, at their respective maximum global stretches, $\lambda_{\max} = 2.9132, 2.6456, 2.2515$ and 1.4308, under loading condition (i). The fringe scales in the deformed configurations

correspond to the maximum principal stretch of each element (representing the level of local deformation), with those having a value of 8 or larger plotted in red. The maximum global and local stretches reached by each mesh are also summarized in Table 12.1. As an additional quantitative comparison, the relevant components of the macroscopic first Piola–Kirchhoff stress $\langle \boldsymbol{P} \rangle$ as functions of the applied global stretch λ or shear γ are shown in Figure 12.13(a)–(b) for loading conditions (i) and (ii). The simulated macroscopic responses are compared with the available analytical solution in the literature for neo-Hookean elastomers, reinforced with a random and isotropic distribution of polydisperse circular particles, which considers the interphasial effect [175, 258].

Several observations and conclusions can be made. First, the macroscopic responses obtained by all three types of meshes under both loading conditions (i) and (ii) agree well with the analytical solutions. Second, the results from the polygonal meshes reach significantly larger global deformation states than the ones from the quadratic triangular mesh. Since the effective volume fraction of the filled elastomer considered in this example is high ($c_p + c_i = 36\%$), resulting in extremely heterogeneous and large localized deformation fields, a remeshing strategy is likely to be ineffective in stretching the triangular mesh farther [284]. Third, the quadratic polygonal meshes exhibit better performance than linear meshes, as they can reach larger global deformation states, especially under loading condition (i). Partially, this is because the quadratic polygonal elements have richer approximating capabilities, allowing them to better capture the curvatures in the highly stretched regions (for example, see the region in Figure 12.12). Furthermore, while producing almost identical macroscopic responses, the quadratic polygonal mesh with the $\mathcal{M}_2 - \mathcal{M}_1$ element in this example appears to reach a larger global stretch than the one with $\mathcal{M}_2 - \mathcal{P}_1^D$ elements under loading condition (i) ($\lambda_{\max} = 2.91$ as compared to $\lambda_{\max} = 2.65$).

12.8.2 Results for a filled silicone elastomer

This subsection studies the large deformation response of a filled elastomer with both its matrix and interphase being a typical silicone rubber, characterized by the

	Max. global deformation		Max. local deformation	
	Pure shear	Simple shear	Pure shear	Simple shear
$\mathcal{M}_1 - \mathcal{P}_0^D$ elements	2.9132	1.086	13.8016	6.4693
$\mathcal{M}_2 - \mathcal{P}_1^D$ elements	2.6456	1.091	11.1457	6.6314
$\mathcal{M}_2 - \mathcal{M}_1$ elements	2.2615	1.078	10.2077	6.9639
CPE6MH elements	1.4308	0.622	4.4819	3.6324

Table 12.1 Comparison of maximum global deformation and the maximum local deformation (maximum principal stretch) in the final deformed configurations obtained by different types of elements. Both matrix and interphase are neo-Hookean materials.

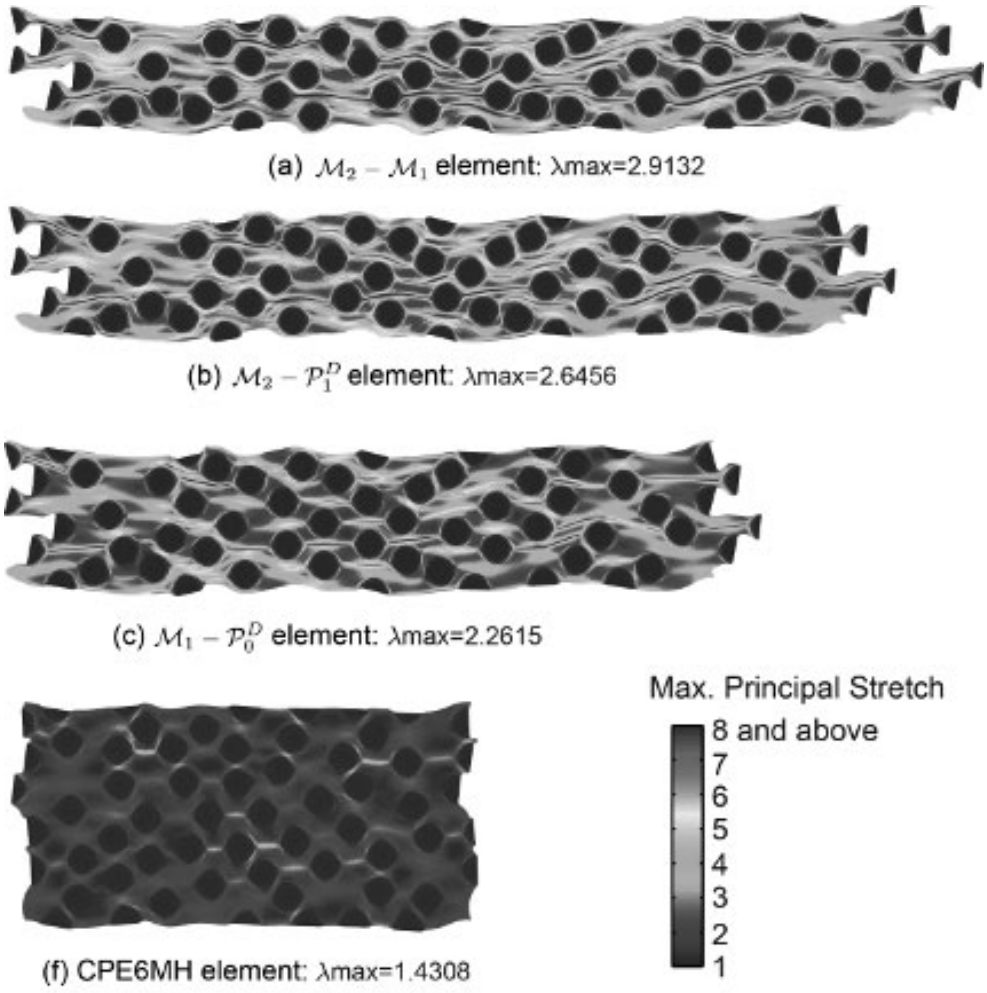

Figure 12.12 For loading condition (i), displaying pure shear with average deformation gradient $\langle \boldsymbol{F} \rangle = \lambda \boldsymbol{e}_1 \otimes \boldsymbol{e}_1 + \lambda^{-1} \boldsymbol{e}_2 \otimes \boldsymbol{e}_2$, $\lambda \geq 1$, the figure illustrates the final deformed configuration reached by (a) $\mathcal{M}_2 - \mathcal{M}_1$ elements, (b) $\mathcal{M}_2 - \mathcal{P}_1$ elements, (c) $\mathcal{M}_1 - \mathcal{P}_0$ elements, and (d) CPE6HM elements (solved in ABAQUS). This figure is adapted from [100]. See color insert.

following stored-energy function [259]

$$W(\boldsymbol{F}) = \begin{cases} \dfrac{3^{1-\alpha_1}}{2\alpha_1}\mu_1[I_1^{\alpha_1} - 3^{\alpha_1}] + \dfrac{3^{1-\alpha_2}}{2\alpha_2}\mu_2[I_1^{\alpha_2} - 3^{\alpha_2}], & \text{if } \det \boldsymbol{F} = 1, \\ +\infty, & \text{otherwise,} \end{cases}$$

with $I_1 = F_{ij}F_{ij}$, $\mu_1 = 0.032$ MPa, $\mu_2 = 0.3$ MPa, $\alpha_1 = 3.837$, $\alpha_2 = 0.559$. Thus, the initial shear modulus of the matrix is $\mu_m = \mu_1 + \mu_2 = 0.332$ MPa, and that of the interphase is $\mu_i = 3.32$ MPa. Again, both loading conditions (i) and (ii) are considered.

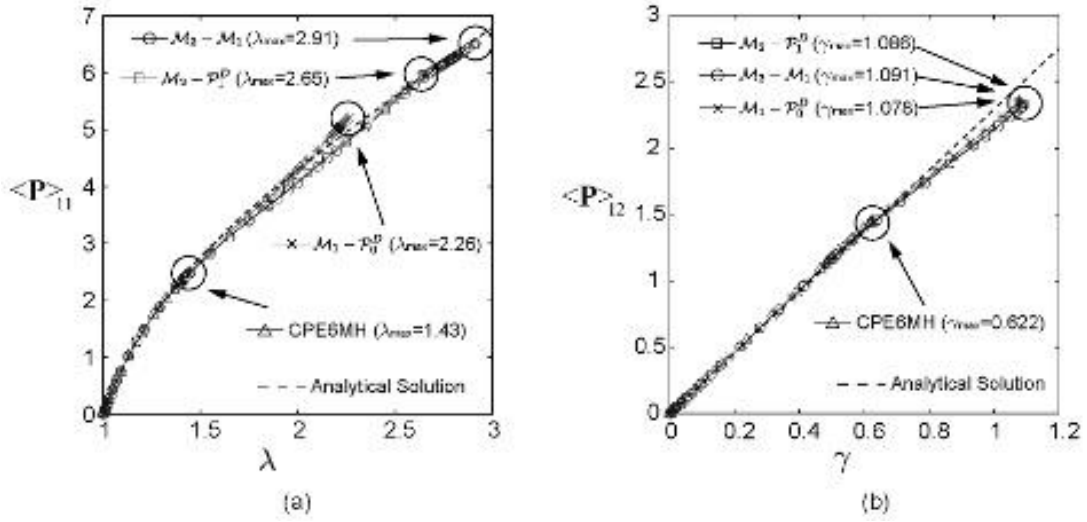

Figure 12.13 Plots of the macroscopic Piola–Kirchhoff stress function as the applied stretch/shear for different types of elements under (a) pure shear ($\lambda \geq 1$) and (b) simple shear.

Figure 12.14(a)–(d) shows the final deformed configurations of the unit cell obtained by $\mathcal{M}_2 - \mathcal{M}_1$, $\mathcal{M}_2 - \mathcal{P}_1^D$, $\mathcal{M}_1 - \mathcal{P}_0^D$, and CPE6MH elements under loading condition (ii) at their respective maximum global deformation states. The color scale in each configuration corresponds to the maximum principal stretch of each element, with those having a value of 4 and above plotted in red. The maximum global and local stretches reached by each mesh are summarized in Table 12.2. Furthermore, the macroscopic responses predicted by each type of element under both loading conditions (i) and (ii) are plotted in Figure 12.15(a) and (b) as functions of applied global stretch λ or shear γ. Similar to the preceding subsection, we conclude that polygonal discretizations (both linear and quadratic elements)

	Max. global deformation		Max. local deformation	
	Pure shear	Simple shear	Pure shear	Simple shear
$\mathcal{M}_1 - \mathcal{P}_0^D$ elements	1.911	1.482	4.256	4.545
$\mathcal{M}_2 - \mathcal{P}_1^D$ elements	2.064	1.548	4.543	4.562
$\mathcal{M}_2 - \mathcal{M}_1$ elements	1.910	1.551	4.257	4.799
CPE6MH elements	1.349	0.595	2.777	2.699

Table 12.2 Comparison of maximum global deformation and the maximum local deformation (maximum principal stretch) in the final deformed configurations obtained by different types of elements. Both matrix and interphase are considered to be typical silicone rubber.

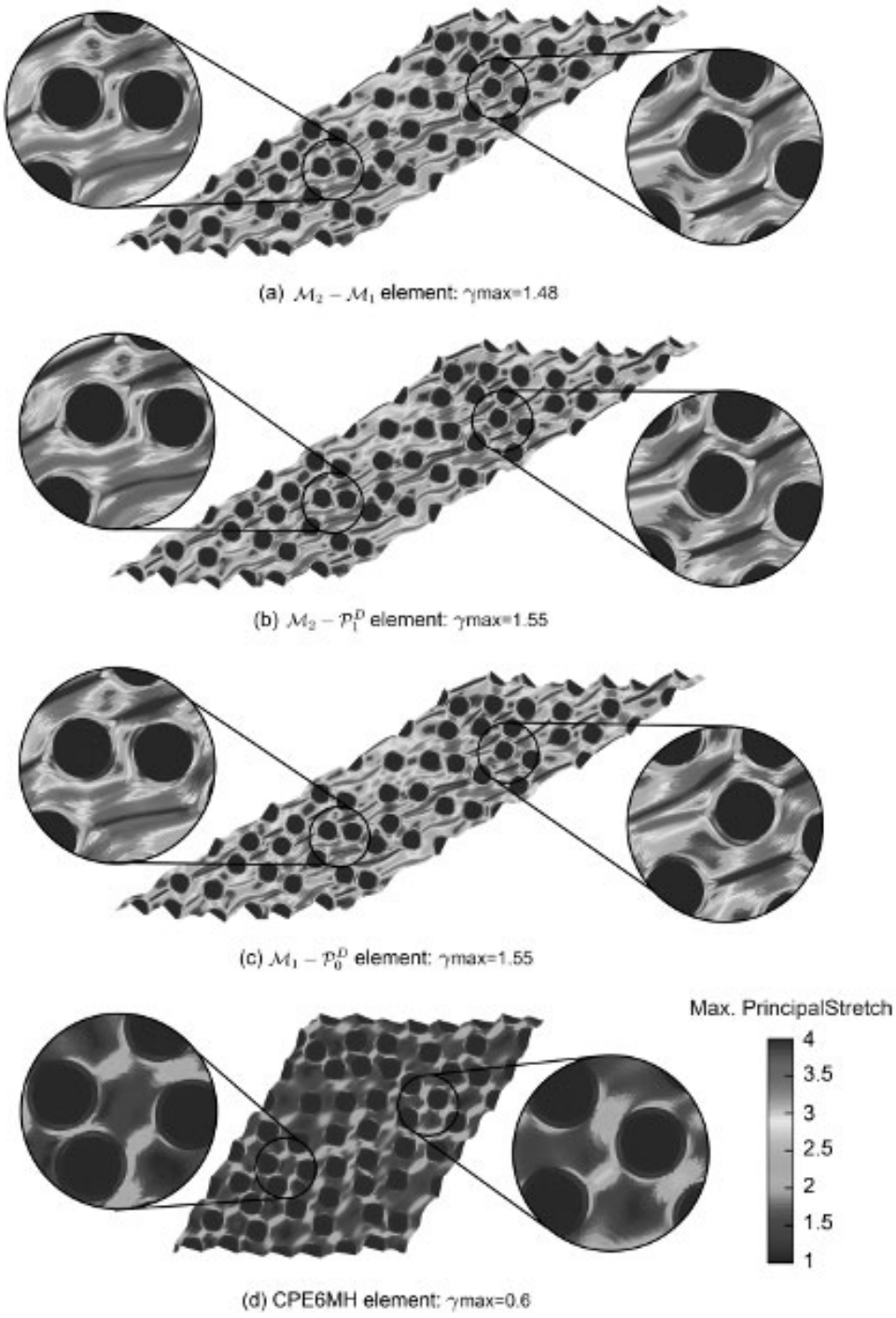

Figure 12.14 For loading condition (ii), displaying $\langle \boldsymbol{F} \rangle = \boldsymbol{I} + \gamma \boldsymbol{e}_1 \otimes \boldsymbol{e}_2$, $\gamma \geq 0$, the figure illustrates the final deformed configurations reached by (a) $\mathcal{M}_2 - \mathcal{M}_1$ elements, (b) $\mathcal{M}_2 - \mathcal{P}_1^D$ elements, (c) $\mathcal{M}_1 - \mathcal{P}_0^D$ elements, and (d) CPE6HM elements (solved in ABAQUS). Both matrix and interphase are considered to be typical silicone rubber. See color insert.

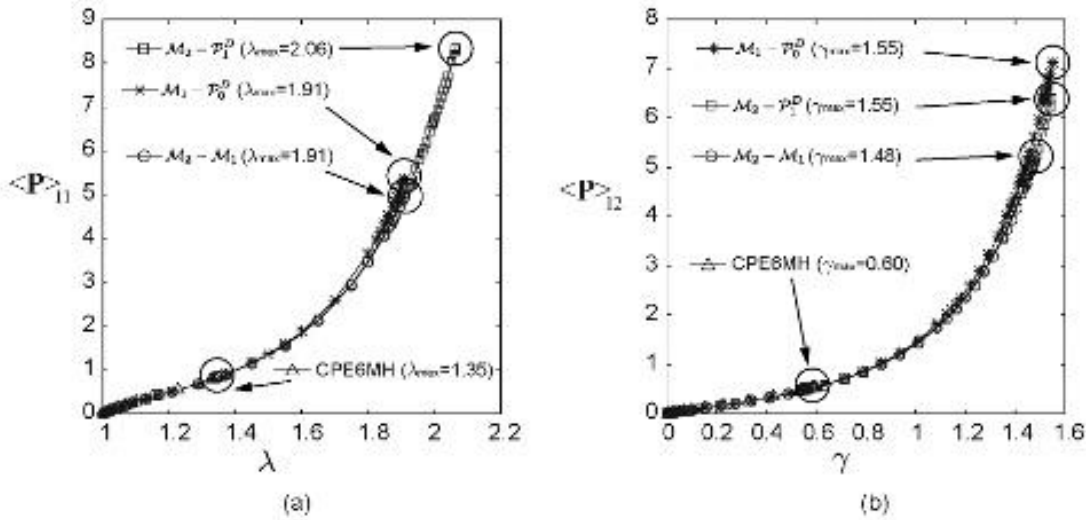

Figure 12.15 Plots of the macroscopic first Piola–Kirchhoff stress as functions of the applied stretch/shear for different types of elements under (a) pure shear ($\lambda \geq 1$) and (b) simple shear. Both matrix and interphase are considered to be typical silicone rubber.

are capable of reaching much larger stretches at both global and local levels than quadratic triangle elements under loading conditions (i) and (ii). However, unlike in the preceding subsection, the quadratic polygonal mesh with $\mathcal{M}_2 - \mathcal{P}_1^D$ elements reaches a larger global stretch than the one with $\mathcal{M}_2 - \mathcal{M}_1$ elements in terms of the maximum global stretch/shear reached. This difference in results indicates that the comparison of performance of the $\mathcal{M}_2 - \mathcal{P}_1^D$ element and $\mathcal{M}_2 - \mathcal{M}_1$ element may be problem-dependent.